

1 Wet-Radome Attenuation in ARM Cloud Radars and Its Utilization in Radar Calibration Using Disdrometer  
2 Measurements

Formatted: Font: 12 pt

Formatted: Justified

3  
4 Min Deng<sup>1</sup>, Scott E. Giangrande<sup>1</sup>, Michael P. Jensen<sup>1</sup>, Karen Johnson<sup>1</sup>, Christopher R. Williams<sup>2</sup>,  
5 Jennifer M. Comstock<sup>3</sup>, Ya-Chien Feng<sup>3</sup>, Alyssa Matthews<sup>3</sup>, Iosif A. Lindenmaier<sup>3</sup>, Timothy G.  
6 Wendler<sup>3</sup>, Marquette Rocque<sup>3</sup>, Aifang Zhou<sup>1</sup>, Zeen Zhu<sup>1</sup>, Edward Luke<sup>1</sup>, and Die Wang<sup>1</sup>

Formatted: Font: Not Bold

7  
8  
9 <sup>1</sup> Brookhaven National Laboratory, Environmental and Climate Sciences Department, Upton,  
10 New York

11 <sup>2</sup> University of Colorado Boulder, Colorado Center for Astrodynamics Research, Boulder,  
12 Colorado

13 <sup>3</sup> Pacific Northwest National Laboratory, Richland, Washington

14  
15  
16 *Correspondence to:* Min Deng (mdeng@bnl.gov)

17  
18  
19 Manuscript to be submitted to AMT publication.

Formatted: Font: 12 pt

35 Abstract

36  
37 A relative calibration technique ~~has been~~ developed for the U.S. Department of Energy's  
38 (DOE) Atmospheric Radiation Measurement (ARM) user facility Ka-Band ARM Zenith Radars  
39 (KAZRs). ~~This method uses the signal attenuation caused by water on the radome to estimate~~  
40 reflectivity factor ( $Z_e$ ) ~~offsets~~. The wet-radome attenuation (WRA) is assumed to follow a  
41 ~~loglinear~~ relationship with rainfall rate ~~during~~ light and moderate rain, ~~as~~ measured by a collocated  
42 surface disdrometer. ~~The technique has an uncertainty of approximately 3 dB, due to factors such~~  
43 ~~as disdrometer measurement error, rain variability between radar and disdrometer sample volumes,~~  
44 ~~and the fitting function's uncertainty for the WRA behavior.~~ A practical advantage of this WRA-  
45 ~~based~~ approach to shorter-wavelength radar monitoring is that, while it requires a reference  
46 disdrometer, it ~~proves feasible~~ for a wider range of collocated disdrometer measurements  
47 ~~compared to traditional direct disdrometer comparison at the onset of light rain. This technique~~  
48 ~~thus offers a~~ cost-effective monitoring tool for remote, ~~or long-term radar~~ deployments.  
49 This ~~calibration~~ technique ~~was~~ applied during the ARM TRacking Aerosol Convection  
50 interactions ExpeRiment (TRACER) from October 2021 through September 2022. The estimated  
51  $Z_e$  offsets ~~were compared~~ against traditional radar calibration and monitoring methods ~~using~~  
52 available ~~datasets from~~ this campaign. ~~Results show that the WRA-based offsets align closely with~~  
53 ~~mean offsets found between cloud radars and from direct disdrometer comparison near the onset~~  
54 ~~of rain, while also reflecting similar offset and campaign-long trends when compared to collocated,~~  
55 ~~independently calibrated radar wind profiler. Nevertheless, overall, the KAZR  $Z_e$  offsets estimated~~  
56 ~~during TRACER remained stable, approximately 2 dBZ lower than the disdrometer estimates from~~  
57 ~~the campaign start until the end of June 2022, after which the offsets increased to around 7 dBZ~~  
58 ~~by the campaign's end. This increase is linked to a drop of about 1 dB in transmitter power toward~~  
59 ~~the conclusion of the project.~~

Deleted: is

Deleted: The technique utilizes

Deleted: due to

Deleted: collected

Deleted: for estimates of the

Deleted: offset

Deleted: logarithmic

Deleted: in

Deleted: conditions,

Deleted: is shown viable

Deleted: than

Deleted: disdrometer

Deleted: comparisons in

Deleted: Adding such techniques may provide an additional,

Deleted: /longer

Deleted:

Deleted: has been

Deleted: in  $Z_e$  are evaluated

Deleted: based on datasets

Deleted: during

Deleted: WRA

87  
88  
89  
90  
91  
92  
93  
94  
95  
96  
97  
98  
99  
100  
101  
102  
103  
104  
105  
106  
107  
108  
109  
110  
111  
112  
113  
114  
115  
116  
117

## Short Summary

A relative calibration technique is developed for the cloud radar by monitoring the intercept of the wet-radome attenuation (WRA) loglinear behavior as a function of rainfall rates in light and moderate rain conditions. This WRA technique is applied to the measurements during the ARM TRACER campaign and reports  $Z_e$  offsets that compare favorably with the traditional disdrometer comparison near the time of rain onset, while also demonstrates similar offset and campaign-long trends with respect to collocated and independently-calibrated reference radars.

## 1 Introduction

The U.S. Department of Energy (DOE) Atmospheric Radiation Measurement (ARM) user facility operates millimeter-wavelength cloud radars (35 and 94 GHz) at various global fixed and mobile sites (e.g., Mather and Voyles, 2013; Miller et al., 2016; Kollias et al., 2007, 2020). These "cloud" radars are often more sensitive than traditional centimeter-wavelength weather radars, allowing them to detect cloud droplets more effectively. However, this sensitivity comes with a trade-off as shorter wavelengths are prone to partial or complete attenuation in clouds and precipitation. Such attenuation introduces uncertainties in key radar-derived properties like reflectivity factor ( $Z_e$ ), affecting cloud and hydrological retrieval accuracy (e.g., Matrosov, 2005; Deng et al., 2014; Zhu et al., 2019).

Given the importance of accurate  $Z_e$  measurements, the routine deployment and operation of cloud radars necessitate frequent calibration and monitoring activities. In general, more rigorous radar calibration efforts can be implemented (e.g., Russchenberg et al., 2020), but these approaches are often system-specific and require highly skilled engineers or technicians, significant time, and specialized equipment (within ARM, e.g., Mead, 2010). For weather and climate applications, radar-based research has increasingly turned to "relative" calibration techniques, which rely on  $Z_e$  estimates from nearby reference instruments or expectations based on intrinsic properties of the hydrometeors or other media (e.g., Bringi and Chandrasekar, 2001; Giangrande et al., 2005; Protat

- Deleted: mean offsets found between the cloud radars and a nearby...
- Deleted: Overall, the KAZR  $Z_e$  offsets estimated during TRACER remains stable and at a level 2 dBZ lower than the  $Z_e$  estimated by disdrometer from the campaign start until the end of June 2022. Thereafter, the radar offsets increase to near 7 dBZ at the end of the campaign.
- Deleted: ¶
- Deleted: multiple
- Deleted: at
- Deleted: frequencies) across a variety of
- Deleted: facilities
- Deleted: .
- Deleted: ;
- Deleted: The popularization of “
- Deleted: ”
- Deleted: for use in atmospheric research is tied to the (... [2])
- Deleted: conventional weather (i.e., cm
- Deleted: )
- Deleted: for detecting
- Deleted: . One
- Deleted: for these radars is that they experience
- Deleted: to potential extinction in
- Deleted: Importantly,
- Deleted: quantitative
- Deleted: property
- Deleted: retrievals from cloud radars often carry an (... [3])
- Deleted: to which its quantities (such as the radar refle (... [4])
- Deleted: Meagher et al., 2006;
- Deleted: , Liu et al., 2022).
- Deleted: necessitates
- Deleted: operationalized
- Formatted: Pattern: Clear
- Deleted: i.
- Deleted: often
- Deleted: an increasing number of “
- Deleted: ”
- Deleted: that include concepts that
- Deleted: of  $Z_e$
- Deleted: instrumentation,
- Deleted: .

176 et al., 2011; Kollias et al., 2019; Maahn et al., 2019; Williams et al., 2023). Several of these  
177 “natural” calibration concepts have proven effective for quantifying radar performance in many  
178 hydrological applications requiring Ze estimates within 2-3 dBZ. The simplest approach is often a  
179 cross-comparison of Ze characteristics with collocated, calibrated reference radars. For example,  
180 extended comparisons of clouds near ARM ground sites using CloudSat radar measurements have  
181 successfully monitored the long-term ARM cloud radar record (Protat et al., 2011; Kollias et al.,  
182 2019). For finer-scale comparisons during ARM deployments, the Ka-Band ARM Zenith Radar  
183 (KAZR) is often collocated with a Radar Wind Profiler (RWP, 915 or 1290 MHz) and the Ka- and  
184 X-band Scanning ARM Cloud Radar (KaSACR/ XSACR), which are easier to monitor using  
185 independent techniques better suited to scanning and/or longer-wavelength radar.

186  
187 Among the various methods of relative cloud radar monitoring, a common approach relies  
188 on surface disdrometer observations. The reflectivity factor can be estimated for assumed rain  
189 properties using techniques such as T-matrix scattering algorithms applied to the drop size  
190 distribution of rain measured by the surface disdrometer (Mishchenko et al., 1996). Comparing  
191 radar-measured reflectivity near the surface with disdrometer-estimated reflectivity provides a  
192 common way to estimate radar calibration offsets (e.g., Kollias et al., 2019; Myagkov et al., 2020;  
193 Russchenberg et al., 2020; and Lamer et al., 2021). Disdrometer comparison techniques like this,  
194 have been implemented as routine procedures for radar monitoring, such as in the Aerosol Cloud  
195 Tracer Gas Research Infrastructure (ACTRIS) network in Europe (Dupont et al., 2022). For radars  
196 that experience negligible attenuation in rain, such procedures are often straightforward to  
197 implement across a variety of widespread precipitating conditions (e.g., Williams et al., 2023).  
198 However, for shorter radar wavelengths, where gaseous attenuation, rain attenuation, and wet-  
199 radome attenuation are not negligible, applying this approach can be more complicated.

200 Specifically, the two-way attenuation associated with radome wetting (referred to here as  
201 wet radome attenuation or WRA) is a well-known phenomenon. During rainfall, water droplets  
202 bead on the surface of the radar radome, forming a wet film that eventually flows off the radome  
203 once it reaches sufficient mass, similar to the water layer on a car window. Droplets impacting the  
204 radome during persistent rain further alter the water depth through bouncing and splashing (Gibble,  
205 1964; Anderson, 1975; Yu et al., 2021). For long-wavelength radars, WRA is often considered  
206 negligible (Thompson et al., 2012; Kurri and Huuskonen, 2008). However, for shorter-wavelength

- Deleted: such...f these “natural” calibration concepts (... [5])
- Deleted: to perform ... cross-comparison of Ze (... [7])
- Formatted (... [6])
- Formatted (... [8])
- Deleted: using...f clouds near ARM ground sites using (... [9])
- Formatted (... [10])
- Deleted: SACR, or ...aSACR and... XSACR) that (... [11])
- Deleted: many forms...arious methods of relative cl (... [12])
- Formatted (... [13])
- Deleted: surface disdrometer-measured
- Formatted (... [14])
- Deleted: The comparison of
- Formatted (... [15])
- Deleted: ( $Z_{e,meas}$ )
- Deleted: ( $Z_{e,dis}$ )
- Deleted: one
- Formatted (... [16])
- Formatted (... [17])
- Formatted (... [18])
- Deleted: path
- Deleted: ,
- Formatted (... [19])
- Deleted: of
- Deleted: sort
- Formatted (... [20])
- Formatted (... [21])
- Formatted (... [22])
- Deleted: for
- Formatted (... [23])
- Deleted: ,
- Formatted (... [24])
- Deleted: under
- Deleted: in rain
- Formatted (... [25])
- Formatted (... [26])
- Deleted: the application of
- Deleted: idea
- Deleted: become
- Deleted:
- Formatted (... [27])
- Formatted (... [28])
- Formatted (... [29])
- Formatted (... [30])
- Deleted: i.e., the...eferred to here as wet radome atte (... [31])
- Formatted (... [32])
- Deleted: and this rain may form...orming a wet film (... [33])
- Deleted: ,
- Deleted: ,
- Deleted: For...owever, for shorter (... [37])
- Formatted (... [34])
- Formatted (... [35])
- Formatted (... [36])

306 radars, the impact of WRA is potentially more significant. For example, at X-band, Bechini et al.  
 307 (2010) and Gorgucci et al. (2013) ~~observed~~ a loss of 5 dB in moderate rain ~~by comparing~~  
 308 simultaneous X-band radar measurements at close range with a collocated video disdrometer. This  
 309 WRA has been shown to depend on the thickness of the water film ( $d$ ) on the radome, which in  
 310 turn is a function of rain rate, ~~as described by~~ the Gibble formula (Gibble, 1964; Anderson, 1975):

311 
$$d = \left( \frac{3\mu_k r R}{2g} \right)^{1/3}, \quad (1)$$

312 where  $\mu_k$  is the kinematic viscosity of water (that also varies with temperature),  $r$  is the radome  
 313 radius,  $R$  is the rain rate, and  $g$  is the gravitational acceleration. Additional relations between WRA  
 314 and  $R$  have been developed based on the Gibble's  $R^{1/3}$  formula by Frasier et al. (2013) and  
 315 Gorgucci et al. (2013) for X-band radar calibration studies.

316 Few studies have considered WRA for assessing cloud radar offsets at Ka-band (35 GHz).  
 317 ~~As~~ the water absorption coefficient is ~~inversely proportional to wavelength~~ (Bertie et al. 1996,  
 318 ~~Segelstein 1981), the WRA at Ka-band is approximately as three times as that at X-band for the~~  
 319 ~~same depth of rainwater on the radome.~~ It is understood that WRA will impact direct estimates of  
 320 the offset between cloud radar and disdrometer  $Z_e$  estimates in rainy conditions, and faulty offset  
 321 assessment after rain ends may occur owing to extended radome drying delays. Therefore, direct  
 322 comparison concepts previously cited typically consider only the periphery cloud, drizzle or light  
 323 rain conditions (i.e.,  $R < 1\text{-}2 \text{ mm hr}^{-1}$ ) at the onset of a rainfall event to minimize various forms of  
 324 attenuation. This often is a very stringent and subjective employment of these conditions: First, it  
 325 limits the opportunities for direct disdrometer monitoring of cloud radar to a selected window of  
 326 rainfall rates and event timing. Identifying these light rain or drizzling conditions is also contingent  
 327 on the requirements for collecting high-quality disdrometer measurements (i.e., those that require  
 328 significant droplet number counts), wherein a separate rain rate cut-off may be required to avoid  
 329 significant WRA. Overall, it is potentially useful to establish other forms of cloud radar monitoring  
 330 that could benefit from a wider range of observations collected during precipitation window.

331 In this study, we ~~first~~ identify intervals of WRA for Ka-band radars by comparing  
 332 observations from ARM's KAZR ~~with~~ a collocated suite of instruments, ~~including~~ a surface  
 333 disdrometer, ~~a~~ calibrated RWP, and ~~KaSACR/XSACR~~ observations collected in vertical pointing  
 334 (VPT) modes during the Tracking Aerosol Convection ~~Interactions Experiment~~ (TRACER). ~~We~~

Deleted: found

Deleted: through comparison of

Formatted: Font: Not Italic

Deleted: through

Deleted: , and

Deleted: At this frequency, one expects a stronger two-way attenuation for the same depth of rainwater on the radome, as

Deleted: approximately three times larger than at X-band

Deleted: .)

Deleted: and

Deleted: SACR

Deleted: interactions ExpeRiment

Deleted: The KaSACR and XSACR radar observations benefit from the radars' ability to shed radome water during scanning, therefore less influenced by

349 then develop a new WRA fitting technique and apply it to calibrate the Ze offset for KAZR using  
350 TRACER measurements. The performance of this technique is evaluated against three traditional  
351 relative calibration or monitoring methods for Ka-band radar: (i) direct disdrometer comparisons  
352 of Ze in light rain at the onset of rain events, (ii) a cross-comparison with independently calibrated  
353 RWP measurements, and (iii) a cross-comparison with collocated scanning KaSACR  
354 measurements.

355 The paper is organized as follows. Section 2 introduces the radar datasets and supporting  
356 TRACER datasets used in this study. In Section 3, a relative calibration technique is developed  
357 with daily KAZR and KaSACR measurements collected during light and moderate rainfall  
358 conditions. In Section 4, the technique is applied to the KAZR measurements during the TRACER  
359 campaign to assess the long-term calibration offset trend for KAZR, and the result is evaluated  
360 against other calibration methods. A summary of the performance of this WRA technique for  
361 relative offset monitoring is provided in Section 5.

## 363 2 TRACER Dataset Description and Comparisons

364 The TRACER campaign took place in the Houston, TX region from 1 October 2021 to 30  
365 September 2022 (Jensen et al., 2019, 2022, and 2023) with a goal of studying the interactions of  
366 aerosols and convective clouds. The main surface measurement site was located at La Porte, TX  
367 housed the deployment of the first ARM Mobile Facility (AMF1; Miller et al., 2016). The AMF1  
368 consists of several ground-based remote-sensing and profiling instruments, and included the  
369 deployment of the KAZR, KaSACR/XSACR, and radar wind profiler (RWP) units that serve as  
370 the radars for this study. The surface instrumentation also included multiple laser and video  
371 disdrometers as reference anchors.

### 373 2.1 TRACER Cloud Radars (KAZR and KaSACR/XSACR)

374 The KAZR (Widener et al., 2012) is a successor to ARM's highly successful millimeter-  
375 wavelength cloud radar (MMCR). The KAZR has a flat radome inclined at 4°. A complete list of  
376 KAZR specifications is provided in Table 1. The KAZR transmits and receives two types of pulses:  
377 (i) the burst pulse, a simple narrow pulse of radio-frequency energy (referred to as "GE" mode),  
378 and (ii) the chirp pulse, a longer, frequency-modulated pulse with higher transmitted energy and  
379 greater sensitivity, but with data collection starting at a higher range due to the larger blind zone

Deleted: . Section 2 introduces the radar datasets and the supporting TRACER datasets used in this study. In Section 3, by implementing a logarithmic relation between WRA and rain rate in light to moderate rain, a relative calibration

Deleted: is developed. This technique monitors

Deleted: intercept of this logarithmic relationship

Deleted: daily

Deleted: collected during WRA conditions into moderate rainfall cases. In Section 4, the technique is applied to the daily KAZR measurements during the TRACER campaign to assess the KAZR long-term calibration offset trend

Deleted: the

Deleted: -

Deleted: measurement

Deleted: measurement. A summary of the performance for these WRA techniques for relative offset monitoring is found in Section 5.

Deleted: ¶

Formatted: Font: Times New Roman, 12 pt, Font colour: Text 1

Formatted: Space Before: 6 pt, After: 6 pt

Deleted: (29° 40' 12'' N, 95° 3' 32.4'' W) that

Deleted: ,

Deleted: , SACR

Formatted: Font: Times New Roman, Font colour: Text 1

Formatted: Font: Times New Roman, Font colour: Text 1

Formatted: Space After: 6 pt

Deleted: follow-on

Deleted: widely

Deleted: ,

Deleted: 4°.

Deleted: listing

Formatted: Font colour: Text 1

Formatted: Font colour: Text 1

Formatted: Font colour: Text 1

Deleted: found

Deleted: which is

Deleted: which is

Deleted: higher

410 imposed by the longer pulse length (referred to as “MD” mode). Although the MD mode is more  
411 sensitive to clouds (i.e., has a lower minimum detectable Ze), only the KAZR GE mode data are  
412 used for disdrometer comparisons, as near-surface observations are required.

413 The KaSACR and XSACR are co-mounted on a scanning pedestal (Kollias et al., 2014a,  
414 2014b). During TRACER, the KaSACR/XSACR typically followed a 10-minute scanning pattern:  
415 (i) two low-level plan position indicator (PPI) scans at 1° and 2° elevation, followed by (ii) 6  
416 hemispheric range height indicator (HSRHI) scans at 30° azimuth intervals, and then (iii) 2 minutes  
417 of vertical pointing (VPT) mode. This study utilizes the 2-minute VPT mode segment from each  
418 10-minute scanning sequence (i.e., nominal scanning VPT mode). The specifications during VPT  
419 mode are listed in Table 1. For one event during the campaign (September 3-4, 2022), the  
420 KaSACR/XSACR was temporarily operated exclusively in VPT mode (i.e., stationary VPT mode)  
421 for radar cross-calibration purposes. The KaSACR has an inclined radome similar to the KAZR,  
422 but is relatively newer, with potentially less deterioration of its hydrophobic coating. The XSACR  
423 has a conical radome with a slant angle of 45° to the surface. Overall, the WRA effect is expected  
424 to be smaller for the XSACR compared to either Ka-band radar, due to wavelength-dependent  
425 differences as well as the improved radome design. The KaSACR calibration offsets between May  
426 and September 2022 are expected to be stable based on ground clutter analysis using relative  
427 calibration adjustment (RCA) techniques (Skolnik, 2000; Hunzinger et al., 2020) and are reported  
428 to be close to 0 dB, according to the ARM TRACER radar b1 data processing report (Feng et al.,  
429 2024).

430 To compare with Ze estimates from VDISQUANTS, radar measurements at 500 m are  
431 selected and corrected for gaseous attenuation using nearby radiosonde measurements (e.g., Ulaby  
432 et al., 1981). Rain attenuation is also corrected using specific attenuation coefficient (K) estimates  
433 from VDISQUANTS, assuming a uniform layer between the surface and 500 m. There is concern  
434 that the radar might saturate, particularly for the KaSACR near its minimum range, which could  
435 introduce a low bias in measured Ze compared to disdrometer Ze. Based on communication with  
436 an ARM radar engineer, the power associated with the highest voltage digitizable by the radar’s  
437 Analog-to-Digital Converter (ADC) is 5.9 dBm. The corresponding KAZR saturation reflectivity  
438 at 500 meters is approximately 45 dBZ, given its calibration constant of -12 dBm. Similarly, the  
439 KaSACR saturation reflectivity at 500 m is about 31 dBZ, given its calibration constant of -26  
440 dBm. The measured radar reflectivities from both KAZR and KaSACR at 500 m are generally less

- Deleted: Though...lthough the MD mode is more ser... [38]
- Formatted [39]
- Deleted: SACR, e.g.,
- Deleted: and
- Formatted [40]
- Formatted [41]
- Deleted: and
- Formatted [42]
- Deleted: nominally repeated
- Formatted [43]
- Deleted: ,
- Formatted [44]
- Deleted: draws
- Formatted [45]
- Deleted: its
- Formatted [46]
- Deleted: scanning
- Deleted: .
- Deleted: for the SACR
- Formatted [47]
- Formatted [48]
- Formatted [49]
- Deleted: modes
- Deleted:
- Formatted [50]
- Deleted: 03-04
- Formatted [51]
- Formatted [52]
- Deleted: SACR
- Deleted: in an
- Deleted: .
- Formatted [53]
- Formatted [54]
- Formatted [55]
- Deleted: the
- Deleted: ...but is relatively newer (i.e.,... with poten... [57]
- Formatted [56]
- Formatted [58]
- Deleted: the
- Deleted: with the
- Formatted [59]
- Formatted [60]
- Deleted: and
- Formatted [61]
- Deleted: .
- Deleted:
- Formatted [62]
- Deleted: be compared
- Formatted [63]
- Deleted: The rain...ain attenuation is also corrected f... [64]

515 than 25 dBZ, well below the saturation threshold. Additional supporting evidence through radar  
516 profile comparisons can be found in the supplementary material.

## 518 2.2 Surface Disdrometer Measurements and Value-Added Products

519 A Parsivel2 laser disdrometer (LDIS) and a two-dimensional video disdrometer (VDIS)  
520 unit were deployed at the main site during TRACER in very close proximity to the cloud radars.  
521 For disdrometer geophysical quantities and data quality control, procedures follow the standard  
522 drop size distribution (DSD) filtering in Giangrande et al. (2019) implemented by ARM in their  
523 precipitation value-added products (Video Disdrometer Quantities--VDISQUANTS and Laser  
524 Disdrometer Quantities--LDISQUANTS, Hardin et al., 2020). These products employ several fall  
525 speed checks, temperature, drop shape/canting assumptions, larger drop restrictions (no drop sizes  
526 > 5 mm) and drop count thresholds (> 20 drops per minute for a valid DSD) that impact estimates  
527 of hydrometeor  $Z_e$  and  $K_r$  for radar frequencies using a T-matrix scattering algorithm (Mishchenko  
528 et al., 1996). As further discussed within the disdrometer literature (Tokay et al., 2001, 2013;  
529 Giangrande et al., 2019; Wang et al., 2021), the VDIS is considered the more reliable and sensitive  
530 disdrometer to a wider range of drop sizes under nominal light rain operating conditions.  
531 Therefore, the estimated  $Z_e$  at Ka-band in VDISQUANTS is used within this study as our ground  
532 truth for KAZR calibration and surface rain rate, while the LDIS products have been used as an  
533 independent reference for monitoring RWP  $Z_e$  estimates (e.g., Williams et al., 2023), which is  
534 required for additional direct radar comparisons in Section 4.

## 536 2.3 Radar Wind Profiler (RWP)

537 The RWP deployed during TRACER was operated using an adaptive scanning mode,  
538 switching between a traditional boundary layer horizontal wind mode and a vertically-pointing  
539 precipitation mode adopted by ARM for its recent deep convective cloud campaigns (e.g., Tridon  
540 et al., 2013; Giangrande et al., 2013, 2016). When the signal-to-noise ratio in the vertical beam  
541 exceeded a predefined threshold, the RWP switched into this precipitation mode and employs a  
542 single vertically-pointing beam operation. This mode transmitted short- and long-pulses to observe  
543 echoes close to the radar with fine resolution, or further from the radar with coarser  
544 resolution. Important to this study, the TRACER RWP mode switching sometimes prevented the  
545 RWP from immediately observing the periphery lightly precipitating clouds as they passed over

**Deleted:** There is a concern that the radar might be saturated, especially for the KaSACR near at its minimum range, which could cause low bias in the measured  $Z_e$  compared to disdrometer  $Z_e$ . Based on a communication with ARM radar engineer, the power associated with the highest voltage digitizable by the radar's Analogue-to-Digital Converter (ADC) is 5.9 dBm. The corresponding KAZR saturation reflectivity at 500 meters is about ~45 dB with its calibration constant of -12 dBm. Similarly, the saturation reflectivity at 500 m is about ~31 dB for KaSACR, with its calibration constant of -26 dBm. While the measured radar reflectivities from both KAZR and KaSACR at 500 m are generally less than 25 dBZ, well below saturation. Further supporting proof through the comparison of radar profiles can be found in Supplemental material. ¶

**Formatted:** Font: Times New Roman, Font colour: Text 1

**Formatted:** Space After: 6 pt

**Deleted:** rain-specific attenuation coefficient (

**Deleted:** )

**Formatted:** Font: Times New Roman, Font colour: Text 1

**Formatted:** Space After: 6 pt



563 the AMF1 site. However, this mode-switching sampling issue does not impact the bulk KAZR-  
564 RWP Ze cross-comparisons because we primarily consider daily average behaviors. As before, the  
565 RWP Ze measurements in precipitation mode were calibrated independently using collocated  
566 LDIS observations (i.e., Williams et al., 2023), who found a standard deviation of 2 - 4 dBZ  
567 between the RWP at 500 m and LDIS.

### 568 3 Cloud Radar Ze Calibration and Monitoring: Development of a New WRA Technique

#### 569 3.1 Identification of WRA: KaSACR/XSACR in Stationary VPT Modes

570  
571 Figure 1a-c show the measured reflectivity ( $Z_e$ ) from the KaSACR/XSACR and the KAZR  
572 GE mode on 03-04 September 2022, when the KaSACR/XSACR was operated exclusively in a  
573 stationary vertically pointing (VPT) mode. Two intervals of widespread rainfall were captured: the  
574 first around 17-19 UTC, and the second from 20-02 UTC. A radar "bright band" signature,  
575 indicative of the melting level, appears around 5 km AGL during this event. After 02 UTC, (20  
576 LT), light rain gave way to high, scattered clouds through the night, until thick anvil clouds from  
577 nearby convection moved in around 15 UTC, (09 LT). Overall, the KaSACR/XSACR reported  
578 similar  $Z_e$  values under peripheral cloudy conditions and during light rain, where rain attenuation  
579 and WRA were minimal. As expected, larger discrepancies between XSACR and KaSACR (with  
580 the KaSACR showing lower, attenuated  $Z_e$  values) occurred during heavier rainfall from 22-00  
581 UTC. The KAZR consistently reported lower  $Z_e$  values than the KaSACR, with differences often  
582 exceeding 5 dBZ throughout the event.

583  
584 The  $Z_e$  difference between the KaSACR and KAZR values in Fig. 1d exhibits strong  
585 temporal variation but limited vertical variation, indicating that the difference is likely driven by  
586 the radar or its local environment (e.g., WRA) rather than atmospheric features. The minimum  
587 difference of ~7 dB in high clouds, observed around 17-18 UTC and again the next morning (15-  
588 17 UTC on 4 September), suggests an overall  $Z_e$  offset between the KAZR and KaSACR. A  
589 minimum difference of ~7 dB in rain (at 19, 21, and 23 UTC) indicates similar WRA behavior for  
590 both KAZR and KaSACR. However, a prolonged increase in this difference after moderate rain,  
591 especially under humid conditions at night (0-12 UTC, or 18-6 LT), suggests that the KAZR and  
592 KaSACR may experience additional discrepancies after rain or in high humidity, possibly due to  
593 the older, less hydrophobic radome of the KAZR, as noted in the Cloud, Aerosol, and Complex  
594

- Formatted ... [65]
- Deleted: ¶
- Formatted ... [66]
- Formatted ... [67]
- Formatted ... [68]
- Formatted ... [69]
- Deleted: SACR
- Formatted ... [70]
- Deleted: XSACR, ...aSACR,...XSACR and the KAZR ... [71]
- Formatted ... [72]
- Deleted: rain ... intervals were captured with ... f wide ... [73]
- Formatted ... [74]
- Deleted: 02UTC
- Formatted ... [75]
- Deleted: was followed by scattering
- Deleted: in
- Deleted: overnight period
- Formatted ... [76]
- Formatted ... [77]
- Formatted ... [78]
- Deleted: other
- Formatted ... [79]
- Deleted: (
- Formatted ... [80]
- Deleted: ,
- Formatted ... [81]
- Deleted: and KaSACR report
- Formatted ... [82]
- Deleted: in the periphery
- Deleted: for initial samples in
- Deleted: when
- Formatted ... [83]
- Formatted ... [84]
- Formatted ... [85]
- Deleted: in rain
- Formatted ... [86]
- Deleted: should be
- Formatted ... [87]
- Deleted: Expectedly, the
- Formatted ... [88]
- Deleted: reporting
- Formatted ... [89]
- Deleted: ) are found
- Formatted ... [90]
- Deleted: the relatively
- Formatted ... [91]
- Deleted: period between 2200-0000
- Formatted ... [92]
- Deleted:  $Z_e$  is
- Deleted: reporting
- Deleted: those from
- Deleted: this difference
- Formatted ... [93]
- Formatted ... [94]
- Formatted ... [95]
- Formatted ... [96]
- Deleted:
- Deleted: . shows a ... exhibits strong temporal variatio ... [97]
- Formatted ... [98]

721 Terrain Interactions (CACTI) campaign (Varble et al. 2021; Hardin et al. 2020). Accurate  
722 correction for KAZR wet-radome attenuation is challenging and beyond the scope of this study.  
723 however, WRA behavior in rain can provide a basis for tracking KAZR calibration, as will be  
724 demonstrated in the following sections.

725 The time series of rain rate ( $R$ ),  $K$  and  $Z_e$  estimates at Ka- and X-bands from  
726 VDISQUANTS for the 03-04 September 2022 case are shown in Fig. 2a and b. The sampled  $R$   
727 from the disdrometer are commonly less than  $1 \text{ mm hr}^{-1}$ , but approach  $5 \text{ mm hr}^{-1}$  around 2330  
728 UTC. The  $Z_e$  from KAZR, KaSACR, XSACR at 500 m are plotted in Fig. 2b. For all collocated  
729 precipitating samples, the XSACR  $Z_e$  (black crosses) has a high correlation with estimated  $Z_e$  ( $r$   
730  $= 0.95$ ), while KAZR  $Z_e$  (blue crosses) are biased low when directly compared to the disdrometer  
731  $Z_e$ , which is exacerbated further in heavy rain contexts. KaSACR  $Z_e$  (red cross) falls in between  
732 XSACR and KAZR  $Z_e$  values.

733 Figure 2c shows the differences between measured and estimated  $Z_e$  ( $Dze$ ) for KAZR,  
734 KaSACR, and XSACR. The XSACR exhibits a minimum  $Dze$  of 0 dB when the rain rate is below  
735  $0.1 \text{ mm hr}^{-1}$ , but this difference can reach 5 dB around 23:30 UTC. The KaSACR  $Dze$  is  
736 approximately 1 dB at 18 and 21 UTC, while the KAZR  $Dze$  is around 7 dB, suggesting calibration  
737 offsets of around 1 dB for KaSACR and 7 dB for KAZR. Both KaSACR and KAZR  $Z_e$  are further  
738 biased lower by an additional 13 dBZ when the rain rate reaches approximately  $5 \text{ mm hr}^{-1}$  around  
739 23:30 UTC. This 13 dB reduction in KAZR and KaSACR estimates is significantly larger than the  
740 expected two-way attenuation in rain at Ka-band ( $\sim 2 \text{ dB}$ , Figure 2a), suggesting that other factors,  
741 such as WRA, contribute increasingly to the observed offset in rain. Additionally, WRA for both  
742 KAZR and KaSACR likely shows similar dependence on rain rate.

743 The estimated  $Z_e$  from VDISQUANTS during the entire TRACER campaign are plotted  
744 as a function of  $R$  in Fig. 3. The estimated  $Z_e$  for both X- and Ka-bands exhibits a log-linear  
745 relationship with  $R$ . When  $R$  exceeds  $2 \text{ mm hr}^{-1}$ , the  $Z_e$  values begin to diverge, and the difference  
746 between the two wavelengths increases as  $R$  rises, likely due to resonance effects associated with  
747 non-Rayleigh scattering (Baldini et al., 2012). The cumulative probability distribution (CDF) of  
748 rain rates (red line in Figure 3) shows that about 15% of disdrometer samples have  $R < 0.1 \text{ mm}$   
749  $\text{hr}^{-1}$ , indicating limited data for traditional direct disdrometer comparison at precipitation onset.  
750 However, approximately 85% of TRACER data samples have  $R < 5 \text{ mm hr}^{-1}$ , suggesting that this

- Formatted ... [105]
- Deleted: CACTI;
- Deleted: ...ccurate correction for KAZR wet-radom ... [107]
- Formatted ... [106]
- Formatted ... [108]
- Formatted ... [109]
- Deleted: , and... XSACR at 500 m are plotted in Fig ... [110]
- Deleted: Fig.
- Formatted ... [111]
- Deleted: has
- Deleted: less than...elow  $0.1 \text{ mm hr}^{-1}$ ,...', but this ... [113]
- Formatted ... [112]
- Formatted ... [114]
- Deleted: (possibly indicating that KaSACR and KA ... [115]
- Formatted ... [116]
- Deleted: decrease...eduction in KAZR and KaSACR ... [117]
- Formatted ... [118]
- Deleted: ...he estimated  $Z_e$  for both X- and Ka-bar ... [119]
- Deleted: is larger than
- Deleted:  $^{-1}$ ,
- Formatted ... [120]
- Formatted ... [121]
- Formatted ... [122]
- Deleted: the
- Deleted: increases
- Deleted: the
- Deleted: of
- Formatted ... [123]
- Formatted ... [124]
- Formatted ... [125]
- Formatted ... [126]
- Deleted: Fig.
- Deleted: the percentage
- Deleted: data
- Deleted: with
- Formatted ... [127]
- Formatted ... [128]
- Formatted ... [129]
- Formatted ... [130]
- Deleted:  $\text{h}^{-1}$  are  $\sim 15\%$ ,
- Deleted: few samples
- Deleted: the application of
- Deleted: ,
- Formatted ... [131]
- Formatted ... [132]
- Formatted ... [133]
- Formatted ... [134]
- Deleted: approximate...pproximately 85 ... of TRA ... [135]

858 large range of data sample is suitable for the WRA technique applications discussed in the  
859 following sections.

### 860 3.2 Identification of WRA: KaSACR/XSACR in its Scanning-VPT Mode

861 To further illustrate the WRA, we compared radar and disdrometer measurements while  
862 the KaSACR/XSACR operated in its nominal 10-minute scanning sequence during a stratiform  
863 rain event observed on 11 August 2022, between 01-04 UTC (Fig. 4). The radars were exposed to  
864 persistent rainfall, ranging from 1 mm hr<sup>-1</sup> at 01 UTC to over 5 mm hr<sup>-1</sup> around 02:15 UTC, leading  
865 to strong radar signal attenuation, particularly visible in the KAZR Ze vertical gradient above 4  
866 km (Fig. 4a). After 03 UTC, the surface rain intensity was so low that the disdrometer could not  
867 effectively measure rain drop size distributions (DSDs) for Ze estimates due to insufficient drop  
868 counts (<20 drops/minute) (Fig. 4b).

869 The disdrometer-estimated surface Ze at Ka- (black diamonds) and X-bands (blue  
870 diamonds) in Fig. 4c consistently show values close to 30 dBZ when rain rates are near 1 mm hr<sup>-1</sup>,  
871 while the KAZR Ze is around 15 dBZ, resulting in a Dze of 15 dB against the disdrometer, as  
872 shown in Fig. 4d. During this event, there is an 8-minute gap in every 2 minutes of VPT  
873 measurements due to the PPI and HSRHI scans. The collocation of the 2-minute VPT data is  
874 extended to a 6-minute window by averaging KaSACR/XSACR and VDISQUANTS data over a  
875 ±2-minute interval.

876 The KaSACR Ze values (red crosses) in Fig. 4c display a sawtooth pattern within each 10-  
877 minute scanning cycle. Each cycle begins with Ze values close to the XSACR Ze, followed by a  
878 decline towards the KAZR Ze value as time progresses, with the scaling possibly related to the  
879 rain rate. In contrast, the 03-04 September 2022 case in Fig. 2b shows parallel Ze trends between  
880 the KAZR and KaSACR. The increasing Dze trend in each 6-minute period (red crosses) in Fig.  
881 4d is more pronounced, indicating that the sawtooth behavior in KaSACR Ze and Dze results from  
882 rainwater accumulation on the radome during the 2 minutes of vertical pointing. If the KaSACR  
883 signal were saturating, it would consistently remain saturated rather than fluctuating. A closer  
884 examination of XSACR Ze and Dze trends (black crosses) in Fig. 4c and d reveals minimal  
885 variability with rain rates across the scanning cycle, likely due to the weaker water absorption  
886 coefficient at X-band and the reduced water accumulation on the conical XSACR radome.

Deleted: to follow

Formatted: Font colour: Text 1

Deleted: ¶

Deleted: SACR

Formatted: Font: Times New Roman, Font colour: Text 1

Formatted: Font: Times New Roman, Font colour: Text 1

Deleted: SACR was operating...he KaSACR/XSACR operated in its nominal 10-minute scanning sequence in...uring a stratiform rain event observed on 11 August 2022, between the hours of ...1 - ...04 UTC (Fig. 4). The radars were under...posed to persistent rain...ainfall, from 1 mm hr<sup>-1</sup>...<sup>1</sup> at 01 UTC to more than...ver 5 r (... [136])

Deleted: which caused ... leading to strong attenuation of the ...adar signal, especially...attenuation, particularly visible in the KAZR Ze vertical gradient above 4 km (Fig. 4a). After 03 UTC, the rain at the ...urface rain intensity was so light...ow that the disdrometer was unable to ...ould not effectively measure rain drop size distributions (DSDs effectively... for Ze estimates due to too few...nsufficient drop counts (<20 drops (<20...minute) (Fig. 4b). (... [137])

Formatted: Not Superscript/ Subscript

Deleted: surface ...isdrometer-estimated surface Ze at Ka- (black diamonds) and X-bands (blue diamonds) shown ...n Fig. 4c are all ...onsistently show values close to 30 dB...BZ when the ...ain rates are near 1 mm hr<sup>-1</sup>,...<sup>1</sup>, while the KAZR Ze is near...round 15 dB (... [138])

Deleted: disdromter of 15 dB...he disdrometer, as plotted...hown in Fig. 4d. As the SACR was operating in its nominal scanning pattern during ...uring this event, there is an 8-minute gap in measurements associated with the PPI and HSRHI scanning sequences for ...very 2 minutes of VPT measurements...due to the PPI and HSRHI scans. The collocation of the 2-minute VPT data is extended to a 6-minute of data with a ±2-minute ...indow by averaging window between SACR ...aSACR/XSACR and VDISQUANTS. ... (... [139])

Formatted: Font: Not Italic

Deleted: cross...rosses) in Fig. 4c display 6-minute... sawtooth behaviors in every ...attern within each 10-minute scanning heartbeat. This pattern starts with values closer to XSACR ...ycle. Each cycle begins with Ze at the beginning of each sawtooth, then it decreases...alues close to the XSACR Ze, followed by a decline towards the KAZR Ze value as time increases...progresses, with the scaling potentially correlated with ...ossibly related to the r (... [140])

Deleted: every...ach 6-minute measurement...eriod (red cross...rosses) in Fig. 4d is more apparent. The sawtooth behaviors of Ze or Dze in KaSACR in this case (... [141])

Formatted: Font: Not Italic

Deleted: trend...rends (black cross...rosses) in Fig. 4c and d,...reveals very little consistent ...inimal variability (... [142])

Formatted: Font: Not Italic

Formatted: Font colour: Text 1

1023 The differing KaSACR patterns between the events in Figures 2 and 4 are associated with  
 1024 rainwater accumulation and the KaSACR/XSACR radar's cycling between scanning and  
 1025 stationary VPT modes. At the start of each scanning VPT period, the radome is covered by a  
 1026 relatively thin film of rainwater, having shed water during the RHI and PPI scans. In VPT mode,  
 1027 excess rainwater rapidly accumulates on the radome, causing increased attenuation. Consequently,  
 1028 WRA for the KaSACR is modulated by the 10-minute scanning cycle. By contrast, during the  
 1029 continuous stationary VPT observations of KAZR and KaSACR on 03-04 September, rainwater  
 1030 accumulated steadily on their radomes, resulting in similar WRA patterns, and the measured Ze  
 1031 and Dze were parallel with a consistent offset of approximately 7 dB.

**Deleted:** from...n Figures 2 and 4 are related to...associated with rainwater accumulation and SACR radar...he KaSACR/XSACR radar's cycling between the ...canning and stationary VPT modes. At the beginning...start of the...each scanning VPT period, the radome is covered with...y a relatively thin film of rainwater since the radome... having shed the ...ater during the RHI and PPI scanning. Excess...cans. In VPT mode, excess rainwater quickly...apidly accumulates... on the radome in the VPT mode... causing enhanced...ncreased attenuation. Therefore, the...nsequently, WRA for the KaSACR is modulated by the 10-minute scanning cycle. Alternatively, for ...y contrast, during the continuous stationary VPT observations of KAZR and KaSACR in its stationary VPT mode ...n 03-04 September, rainwater accumulated steadily on their radomes in a consistent/continuous way, therefore the ... resulting in similar WRA patterns are similar (... [143])

**Deleted:** are...ere parallel to each other ...ith a constant...onsistent offset of about...pproximately (... [144])

**Formatted:** Font: Not Italic

**Formatted:** Font: Times New Roman, Font colour: Text 1

### 1033 3.3 WRA Fitting Calibration Technique

1034 In this section, we examine the WRA behavior toward developing a relative calibration  
 1035 technique for cloud radar monitoring. Figure 5a shows the estimated Ze by KaSACR at 500 m  
 1036 (black cross) after gaseous and rain attenuation corrections and the corresponding VDISQUANTS-  
 1037 estimated Ze (red cross) as a function of R for the 03-04 September case. A very well-correlated  
 1038 monotonic relationship between the VDISQUANT-estimated Ze and R in logarithmic space is  
 1039 observed. However, the KaSACR-measured Ze is biased low relative to the estimated Ze, and the  
 1040 offset ( $Dze = Ze_{dis} - Ze_{meas}$  shown in Fig. 5b) with increasing R. The Dze approaches 0 dB at  
 1041  $R < 0.1 \text{ mm hr}^{-1}$ , when minimal WRA is expected due to the limited water on the radome. However,  
 1042 Dze increases up to 15 dB at  $R \sim 5 \text{ mm hr}^{-1}$ , which is potentially a disadvantage when considering  
 1043 cloud radar observations in precipitation. However, this characteristic range of WRA relative to R  
 1044 provides an opportunity for exploring relative radar calibration techniques.

**Deleted:** (black cross) ...y KaSACR at 500 meter... (black cross) after gaseous and rain attenuation corrections and the corresponding VDISQUANTS-estimated Ze (red cross) as a function of rain rates... for the 03-04 September case. A very well-correlated monotonic relationship between the VDISQUANT-estimated Ze and R in logarithmic space is observed. However, the KaSACR-measured Ze is biased low compared...relative to the estimated Ze, and the offset between them (... [145])

**Deleted:** increases as...ith increasing R increases... The Dze is near...pproaches 0 dB at  $R < 0.1 \text{ mm hr}^{-1}$ , when water films may not form on the radome – thus, ...inimal WRA is expected...due to the limited water on the radome. However, Dze increases up to 15 dB at  $R \sim 5 \text{ mm hr}^{-1}$ . The WRA with magnitude up to 15 dB (... [146])

**Formatted:** Font colour: Text 1

**Deleted:** magnitude and...haracteristic range of attenuation as a function of ...RA relative to R provides a unique...n opportunity to explore...or exploring relative radar calibration techniques. (... [147])

**Deleted:** we can perform...a weighted linear least-squares fitting...it of the Dze with R in logarithm can be applied, as described in the following Eq...uation 2: (... [148])

1046 Given a quasi-linear correlation between Dze and R in logarithmic space in Fig. 5b, a  
 1047 weighted linear least-squares fit of the Dze with R in logarithm can be applied, as described in  
 1048 Equation 2:

$$Dze = a + b \log(R) \quad (2)$$

1051 For the cases shown in Fig. 5b, the fitted slope b is estimated to be 8.6. The intercept "a" captures  
 1052 the radar calibration offset and the WRA when R is 1 mm hr<sup>-1</sup>. Given the KaSACR calibration  
 1053 offset is close to 0, the intercept primarily reflects WRA at this rain rate, yielding an intercept of  
 1054 approximately 11.1 dB.

**Deleted:** are...s estimated to be 8.6. The intercept "a" captures the radar calibration offset and the WRA when R is 1 mm hr<sup>-1</sup>. As...iven the KaSACR calibration offset is close to 0 then... the intercept due to the...rimarily reflects WRA effect with R equal to 1 mm hr<sup>-1</sup> is around...t this rain rate, yielding an intercept of approximately 11.1 dB. (... [149])

**Formatted:** Indent: First line: 0"

1151 This log-linear relation between  $Dze$  and  $R$  is different from the  $R^{1/3}$  dependence described  
 1152 by Gibble's formula (Eq.1), which is applied by Frasier et al. (2013) and Gorgucci et al. (2013) in  
 1153 X-band radar calibrations. Since the water absorption coefficient at Ka-band is approximately three  
 1154 times that at X-band, we divide the result of Equation 2 by 3 and compare it with the fitting  
 1155 relations from Frasier et al. (2013, solid blue line) and Gorgucci et al. (2013, solid black line) in  
 1156 Figure 6. The relationship from this study intersects with those of Frasier et al. (2013) and Gorgucci  
 1157 et al. (2013) at  $R=0.2$  mm hr<sup>-1</sup>, aligning with the majority of our data. When  $R > 0.2$  mm hr<sup>-1</sup>, our  
 1158 WRA fitting results exceed those of Gorgucci et al. (2013) by less than 0.5 dB, although Gorgucci  
 1159 et al.'s relation is 0.5-1 dB higher than that of Frasier et al. (2013). When  $R < 0.2$  mm hr<sup>-1</sup>, our  
 1160 WRA fitting result is 0.5-1 dB lower than both previous studies. The observed differences (within  
 1161 1 dB) are smaller than the data scatter in Fig. 5b (standard deviation of 3 dB) and the discrepancies  
 1162 between the two previous studies, suggesting that the log-linear fitting in Equation 2 is suitable for  
 1163 WRA correction when  $R$  is below 5 mm hr<sup>-1</sup>, the selected threshold for our analysis. The  
 1164 calibration offset calculation associated with the WRA fitting functions will be further examined  
 1165 in Section 4.

1166  
 1167 Assuming that radar calibration offsets are independent of  $R$ , and that WRA depends  
 1168 intrinsically on  $R$ , the radar calibration offset can be determined by monitoring the fitted intercept  
 1169 in Equation 2. Figure 5c shows the fitted intercept of  $Dze$  of KAZR is 18.5 dB, about 7.5 dB higher  
 1170 than that of KaSACR, which is consistent with the observed offset between KaSACR and KAZR  
 1171 in Figure 1d and the time series in Figure 2c. Alternatively, we can also assume negligible WRA  
 1172 at very low rain rates, e.g.,  $R = 0.05$  mm hr<sup>-1</sup>, making  $Dze (R = 0.05)$  a reliable measure of the radar  
 1173 calibration offset ( $C$ ) for monitoring radar performance. For the KaSACR on 03-04 September  
 1174 case (Fig. 5a), the  $Dze (R = 0.05)$  is -0.1 dB, while for the KAZR, it is 7.3 dB, consistent with  
 1175 direct comparisons between KaSACR, KAZR, and VDISQUANTS. This finding suggests that the  
 1176 WRA technique provides robust offset estimates for this case. The corrected  $Ze$  values using the  
 1177 log-linear fitted  $Dze$  in Eq. 2 are compared with VDISQUANTS  $Ze$  in Fig. 5c and 5f for KaSACR  
 1178 and KAZR, respectively. The correlation coefficient ( $r$ ) improves to  $\sim 0.9$ , with a mean bias of 0  
 1179 dB and a standard deviation of 3.0 dB for both KaSACR and KAZR.

- Deleted: of  $R^{1/3}$  ...Eq.1) ... [150]
- Deleted: for ... [151]
- Formatted ... [151]
- Formatted ... [152]
- Deleted: As ... [153]
- Deleted: about ... [153]
- Formatted ... [153]
- Formatted ... [154]
- Deleted: Eq. 2 of the log-linear fitting ... [154]
- Deleted: plot ... [155]
- Formatted ... [155]
- Formatted ... [156]
- Deleted: in ... [156]
- Deleted: ; ... [157]
- Deleted: ; ... [157]
- Formatted ... [157]
- Formatted ... [158]
- Formatted ... [159]
- Deleted: We find that the ... [160]
- Deleted: derived in ... [160]
- Formatted ... [160]
- Formatted ... [161]
- Deleted: of ... [161]
- Deleted: where...aligning with the majority of the... [163]
- Deleted: this...ur WRA fitting result is larger than... [165]
- Formatted ... [162]
- Formatted ... [164]
- Deleted: less than...elow 5 mm hr<sup>-1</sup>, previously ... [167]
- Deleted: as the ... [166]
- Deleted: data of interest ... [166]
- Formatted ... [166]
- Formatted ... [168]
- Formatted ... [169]
- Formatted ... [170]
- Deleted: As the ... [171]
- Deleted: assumed ...ndependent of  $R$ , and the WRA ... [171]
- Formatted ... [172]
- Deleted: to...ith the observed offset between KaSA ... [173]
- Deleted: ¶ ... [175]
- Formatted ... [174]
- Deleted: the ...DISQUANTS  $Ze$  in Fig. 5c and f ... [177]
- Formatted ... [176]
- Formatted ... [176]
- Deleted: increases...mproves to  $\sim 0.9$ , the...ith a me ... [179]
- Formatted ... [178]
- Formatted ... [180]

1369 To further explore the intrinsic WRA dependence on  $R$ , we applied the WRA log-linear  
 1370 fitting calibration technique to KaSACR in its scanning-VPT modes. Due to water shedding during  
 1371 the scanning cycle, we used the last-minute measurement of each 2-minute VPT period within the  
 1372 10-minute scanning cycle. To obtain a range of samples, we identified five stratiform rain days—  
 1373 May 25, August 5, 11, 19, and 29—and combined data from these events. The data collected from  
 1374 those five days are plotted along with the corresponding VDISQUANTS-estimated  $Z_e$  (red cross)  
 1375 as a function of rain rates in Fig. 5g. For these events,  $Dze_{(R=0.05)}$  is -0.9 dB, with slope “b” fitted  
 1376 to 8.6. The corrected  $Z_e$  using this log-linear fitted  $Dze$  is compared with the VDISQUANTS  $Z_e$   
 1377 in Fig. 7i, demonstrating a strong correlation with the reference  $Z_e$ , along with a smaller standard  
 1378 deviation ( $r=0.91$ ; mean bias, 0 dB; and standard deviation, 2.0 dB).

1379 Recall the  $Dze_{(R=0.05)}$  of -0.1 dB for stationary VPT mode in 03-04 September case, the  
 1380 difference between the two KaSACR offsets is less than 1 dB, which is well within the standard  
 1381 deviation of the estimated  $Z_e$  (3 dB) as a function of  $R$ , and aligns closely with the 1 dB offset  
 1382 from the direct disdrometer comparison at light rain onset in Fig. 2. This suggests that the  $R$   
 1383 dependence of WRA is a valid assumption, therefore the interceptor or  $Dze_{(R=0.05)}$  in the fitting of  
 1384 Equation 2 can be a useful metric for radar offset monitoring.

1385 The time and height plots of  $Z_e$  from KaSACR, XSACR, and KAZR GE and MD modes  
 1386 on 03-04 September 2022 (after the WRA correction is applied) are shown in Figure 7. For the  
 1387 precipitating period, KaSACR is adjusted with Eq. 2 with a slope of 8.6 and constant of 11.1 (Table  
 1388 2 or Fig. 5b). XSACR is modified with the offset of 3 dB from VDISQUANTS (black cross in Fig  
 1389 2d), and KAZR GE mode is corrected using Eq. 2 with a slope of 8.6 and an intercept of 18.5  
 1390 (Table 2, or Fig. 5b). For non-precipitating periods, the calibration offsets for KaSACR and  
 1391 XSACR are assumed to be 0 dB based on the previous discussion, while the KAZR GE mode is  
 1392 calibrated with an offset of 7 dB. In contrast to the apparent difference of more than 5 dB between  
 1393 KAZR and KaSACR shown in Figure 1, the corrected  $Z_e$  values from KAZR and KaSACR are  
 1394 comparable to those from XSACR in cloud and light rain conditions. Under the relatively heavy  
 1395 rain conditions (e.g., 2330 UTC), XSACR  $Z_e$  along the fall streaks maintains magnitudes near 30  
 1396 dBZ from the surface up to the melting layer, while  $Z_e$  estimates from KAZR and KaSACR  
 1397 gradually decrease from the surface to the melting layer, likely due to increasing attenuation in  
 1398 Ka-band observations. This comparison in Figure 7 further supports the applicability of the WRA

Deleted: can apply this

Deleted: in

Formatted: Font colour: Text 1

Formatted: Font colour: Text 1

Deleted: use

Deleted: every...ach 2-minute VPT period in...ithin the 10 minutes...minute scanning heartbeat...ycle. To provide...btain a variety...ange of samples, we identified 5...ive stratiform rainy...ain days observed on ...May 25, August 05..., 11, 19, and 29 ...and combined data from these events together... The data collected data ...rom those 5...ive days are plotted along with the corresponding VDISQUANTS-estimated  $Z_e$  (red cross) as a function of rain rates in Fig. 5g. For these events,  $Dze_{(R=0.05)}$  is -0.9 dB, with slope “b” fit...itted to 8.6. The adjusted...orrected  $Z_e$  using this log-linear fitted  $Dze$  is compared with the VDISQUANTS  $Z_e$  in Fig. 7i is found to be well-correlated...i, emonstrating a strong correlation with the reference  $Z_e$ , along with a smaller standard deviation ( $r=0.91$ , 0 dB... mean bias, 0 dB; and 2.0 dB ...tandard deviation).

[181]

Formatted: Font colour: Text 1

Deleted: in...f -0.1 dB for stationary VPT mode in 03-04 September case is -0.1 dB... the difference between the two KaSACR offsets is less than 1 dB, which is well within the standard deviation of the estimated  $Z_e$  (3 dB) as a function of  $R$ , and is close to...ligns closely with the 1 dB offset from the direct disdrometer comparison at light rain onset in Fig. 2. This suggests that the  $R$  dependence of WRA is a valid assumption, therefore the interceptor or  $Dze_{(R=0.05)}$  in the fitting Eq...f Equation 2 can be a useful metric for radar offset monitoring.

[182]

Deleted: appying...ith a slope of 8.6 and constant of 11.1 (Table 2 or Fig. 5b). XSACR is modified with the offset of 3 dB from VDISQUANTS...DISQUANTS (black cross in Fig 2d), and KAZR GE mode is corrected using Eq. 2 with a slope of 8.6 and an intercept constant ...f 18.5 (Table 2, or Fig. 5b). For non-precipitating periods, the calibration offsets for KaSACR and XSACR are assumed to be 0 dB based on the previous discussion, while the KAZR GE mode is calibrated with an offset of 7 dB. Compared...n contrast to the apparent difference of more than 5 dB between KAZR and KaSACR suggested...hown in Figure 1, the corrected  $Z_e$  values from KAZR and KaSACR are similar...omparable to those from XSACR in clouds...loud and light rain conditions. Under the relatively heavy rain conditions (see, e.g., 2330 UTC),  $Z_e$  in ...SACR  $Z_e$  along the fall streaks retains...aintains magnitudes ~...ear 30 dBZ from the surface up to the melting layer, while  $Z_e$  estimates from KAZR and KaSACR gradually decrease from the surface to the melting layer, presumably...ikely due to accumulating...ncreasing attenuation in rain in ...a-band observations. This comparison in Figure 7 further supports the idea that

[183]

1582 fitting technique to KAZR measurements and KaSACR in VPT modes, providing reasonable  
1583 estimates for wet-radome corrections during precipitation and radar offset monitoring.

**Deleted:** can be applied ...o KAZR measurements and KaSACR in VPT modes, and can provide...roviding reasonable estimates for wet-radome corrections in rain or during precipitation and radar offsets (... [184])

**Formatted:** Indent: First line: 0.5"

#### 1585 4 Application and Evaluation of the WRA Offset Monitoring During TRACER

**Formatted:** Font colour: Text 1

##### 1586 4.1 Daily TRACER KAZR Calibration Offset Applications

**Formatted:** Space After: 6 pt

**Formatted:** Font: Times New Roman, Font colour: Text 1

**Formatted:** Space Before: 0 pt, After: 6 pt

1588 We apply the WRA fitting technique on the  $Dze$  and  $R$  relationship using VDISQUANTS  
1589  $Ze$  estimates versus KAZR  $Ze$  for each day with measured precipitation throughout TRACER  
1590 campaign. The fitted slopes from the daily events typically range from 6 to 10, with  $rr$  generally  
1591 exceeding 0.7. The fitted slopes and associated fitting errors depend on the distribution of data  
1592 samples. For example, in rain events with short durations or limited variability in intensity, data  
1593 samples may cluster within a narrower range, resulting a relatively lower correlation coefficient  
1594 between the fitted  $Ze$  and disdrometer  $Ze$ , potentially indicating less reliable results.

**Deleted:** perform...pply the WRA fitting technique on the  $Dze$  and  $R$  relationship using VDISQUANTS  $Ze$  estimates versus KAZR  $Ze$  for each day with measured precipitation over the entire...hroughout TRACER campaign. The fitted slopes from the daily events typically range from 6 to 10, with  $rr$  typically larger than...enerally exceeding 0.7. The fitted slopes and associated fitting errors depend on the data sample ...istribution...of data samples. For example, for...n rain events with short durations or limited intensity variability, the...in intensity, data samples may cluster in...ithin a narrower range, thus the fitted  $Ze$  may suggest...resulting a relatively lower correlation coefficient with...etween the fitted  $Ze$  and disdrometer  $Ze$  and be considered (... [185])

1596 To mitigate uncertainty associated with "daily" fitting as above, one may assume that the  
1597  $Dze$  and  $R$  relation has a constant slope over longer windows. In this study we consider applying  
1598 the WRA fitting technique with an average slope of 8, selected as a representative value for  
1599 extended rain conditions across the entire TRACER campaign dataset. As a sensitivity study of  
1600 this composite slope, we conduct offset calculations with proxy slope values at 6, 8 and 10 for both  
1601 KAZR and KaSACR in the 03-04 September 2022 case. Table 2 presents the results of these tests.  
1602 As the slopes increase from 6 to 10, the calibration offsets for both KAZR and KaSACR decrease  
1603 by approximately 3 dB, as expected. With increasing slope values, the least-squares fit prioritizes  
1604 the data samples around 0.1 - 1 mm  $hr^{-1}$ , resulting in a mathematical decrease in  $C$ .

**Deleted:** avoid...itigate uncertainty associated with "daily" fitting as above (and/or lack of sampling therein associated with additional daily spread),... one may assume that the  $Dze$  and  $R$  relation has a constant slope over longer windows. Here...n this study we consider applying the WRA fitting technique with an average slope of 8, as a value ...elected to be...s a representative value for extended rain conditions over...cross the entire TRACER campaign dataset. As a sensitivity study of this composite slope choice... we perform these...onduct offset calculations with proxy slope values at 6, 8 and 10 for both KAZR and KaSACR on...n the 03-04 September 2022 case. The ...able 2 presents the results for...f these tests are shown in Table 2... As the slopes increase from 6 to 10, both ...he KAZR and KaSACR calibration offsets for both KAZR and KaSACR decrease by by about...pproximately 3 dB, as expected. As the ...ith increasing slope value increases, to minimize...alues, the least square fitting for the majority of...squares fit prioritizes the data sample located...amples around 0.1 - 1 mm  $hr^{-1}$ ,  $C_{(R=0.05)}$  must mathematically...<sup>1</sup>, resulting in a mathematical decrease. As a (... [186])

1605 To further illustrate, we applied the WRA fitting with a slope of 6 to the KaSACR  
1606 observations in Figure 5a. The fitted relation is represented by the red dashed line in Figure 6. It  
1607 can be seen that the fitted  $Ze$  with a slope of 6 lies between the results from Frasier et al. (2013)  
1608 and Gorgucci et al. (2013). For most data samples (concentrated around 0.1 - 1 mm  $hr^{-1}$ ), the  
1609 difference between the two WRA fitting results remains within 1 dB. The resulting  $C$  with slope  
1610 of 6 is larger than that with a slope of 8. However, the offset deviation due to possible fitting slope,  
1611 fitting changes (shown in Table 2) is 3 dB, which is within the standard deviation of the estimated  
1612  $Ze$  as a function of  $R$  (~3 dB). Therefore, even with fitting slope errors associated with this relative

**Deleted:** illustration...llustrate, we performed...plied the WRA fitting with a slope of 6 for...o the KaSACR observations in Figure 5a. The fitted relation is plotted as...epresented by the red dashed line in Figure 6. One finds...t can be seen that the fitted  $Ze$  with a slope of 6 lies between the results from Frasier et al. (2013) and Gorgucci et al. (2013). For most of the ...ata samples (located...oncentrated around 0.1 - 1 mm  $hr^{-1}$ ), the  $C$  (... [187])

**Formatted:** Subscript

**Deleted:** -fit change (...fitting changes (shown in Table 2) is 3 dB and... which is within the standard deviation of the estimated  $Ze$  as a function of  $R$  (~3 dB). Thus...herefore, even with slope (... [188])

1819 WRA technique, drifts larger than the 3 dB in the long-term calibration trend would be meaningful  
1820 and identifiable.

1821 The calculated KAZR calibration offsets during the entire TRACER campaign are shown  
1822 in Fig. 8a (black asterisk for the daily value, thin dash line representing the mean campaign-wide  
1823 trend). The calibration offsets remain relatively stable around 2 dB with a standard deviation of 3  
1824 dB until 1 July 2022 (273 days since 1 Oct. 2021 in Fig. 12). After this date, the calibration offset  
1825 increases to around 7 dB in September. This shift is larger than the uncertainty of the fitting method  
1826 and the standard deviation of the fitting data, which is found to be linked to a drop of about 1 dB  
1827 in transmitter power toward the end of the project in TRACER radar b1 data processing (Chen et  
1828 al., 2024)

1829  
1830

#### 1831 4.2 Evaluation of the TRACER KAZR Calibration Trend

1832 By monitoring the  $Dze_{(R=0.05)}$  from each rainy day that meets our stratiform and duration  
1833 selection criteria, we determine a relative radar calibration offset trend. This offset includes  
1834 additional uncertainty due to fitting uncertainty and the assumption of negligible WRA at  $R \sim 0.05$   
1835 mm hr<sup>-1</sup>. Combining this WRA fitting technique with other, typically less frequent, absolute radar  
1836 calibration references would be ideal and cost-effective for KAZR long-term calibration. To  
1837 evaluate the KAZR calibration offset trend over the entire TRACER campaign, we performed  
1838 three separate tests to demonstrate the potential offset uncertainty and/or advantages of the current  
1839 WRA fitting technique compared to other established methods.

1840

##### 1841 4.2.1 Direct KAZR-Disdrometer Comparison Near to Light Rain Onset

1842 As previously noted, a wet radome film may not form immediately at the onset of light  
1843 rain, so WRA is often assumed to be negligible when calibrating radar using disdrometer  
1844 measurements near these rain onset windows. We perform a direct KAZR-disdrometer comparison  
1845 at or near light rain onset for qualifying KAZR calibration events. The onset mean offset for each  
1846 day is calculated if there are data samples with  $R < 0.1$  mm hr<sup>-1</sup> lasting for 5 consecutive minutes  
1847 within each observed rain event. The onset mean offsets are shown in Fig. 8a (red diamonds). For  
1848 days with an onset mean offset, these values are typically close to those calculated using the WRA  
1849 fitting technique. However, this method's applicability depends on the variation in precipitation

Deleted: most  
Deleted: resulting  
Deleted: larger than the 3 dB

Deleted: for  
Deleted: We find that the  
Deleted: are  
Deleted: at  
Deleted: that time  
Deleted: This late-period offset drift exceeds 5 dB, probably due to deterioration of radar components in heavy rains in July and August.  
Deleted: .

Formatted: Font colour: Text 1

Formatted: Font: Times New Roman, Font colour: Text 1

Formatted: Space After: 6 pt

Deleted: every

Deleted:

Deleted: has an

Deleted: associated with its

Deleted: The combination of

Deleted: the

Deleted: during

Deleted: advantage

Deleted: as

Formatted: Indent: First line: 0.5"

Formatted: Font: Times New Roman, 12 pt, Italic, Underline, Font colour: Text 1

Formatted: Space After: 6 pt

Deleted: mentioned

Deleted: therefore the

Deleted: /

Deleted: in rain events

Deleted: of

Deleted: from

Deleted: in the day

Deleted: the

Deleted: the offsets from

Deleted:

Deleted: the application of

Deleted: method



1883 rate over the 5-minute sampling period and the minimum sensitivity of VDISQUANTS. The  
1884 former introduces large uncertainty, while the latter limits the number of data samples, as shown  
1885 in Fig. 8a.

**Deleted:** VDISQUANTS ...imum sensitivity...of VDISQUANTS. The former causes...ntroduces large uncertainty and... while the latter causes fewer...imits the number of data samples, as shown in Fig. 8a. (... [189])

**Formatted:** Indent: First line: 0.5"

#### 1887 4.2.2 WRA Fitting Technique Against the Calibrated RWP Ze

**Formatted:** Font: Times New Roman, 12 pt, Italic, Underline, Font colour: Text 1

**Formatted:** Space After: 6 pt

1888 As an independent cross-comparison, we also apply the WRA fitting technique with respect  
1889 to calibrated RWP Ze at RWP time resolution (less than 8 seconds), using interpolated disdrometer  
1890 rain rates over the entire TRACER campaign. Here, Dze is replaced by the difference between  
1891 KAZR and RWP measurements. The WRA calibration offsets using RWP measurements are  
1892 shown with black asterisks in Fig. 8b. First, we observe fewer available RWP data points, due to  
1893 RWP mode switching during transient rain events. For days with available RWP measurements,  
1894 the calibration offsets closely align with those derived using disdrometer-estimated Ze in Fig. 8a  
1895 and direct disdrometer comparisons. The offset trend drift from early July to September is  
1896 smoother and more clearly defined than the trend observed with disdrometer measurements, likely  
1897 due to better temporal resolution. Overall, the consistency in temporal trend and magnitude of  
1898 calibration offsets between disdrometer and RWP measurements indicates strong performance of  
1899 the new WRA fitting technique.

**Deleted:** perform...pply the WRA fitting technique with respect to calibrated RWP Ze at RWP time resolution (less than 8 s) with ...econds), using interpolated disdrometer rain rates over the entire TRACER campaign. Now the...ere, Dze is replaced with...y the difference between KAZR and RWP measurements. (... [190])

**Formatted:** Indent: First line: 0.5"

#### 1901 4.2.3 Cross-Comparison Between KaSACR and KAZR

**Formatted:** Font: Italic, Underline, Font colour: Text 1

**Formatted:** Normal, Justified, Line spacing: 1.5 lines

1902 As previously mentioned, KaSACR calibration offsets remained stable between May and  
1903 September 2022. Furthermore, its calibration offsets, calculated from the WRA fitting technique  
1904 with scanning VPT and stationary VPT measurements in Fig. 6, are approximately -0.9 to -0.1 dB,  
1905 respectively, and around 1 dB from direct disdrometer comparison at light rain onset. We  
1906 tentatively assign a calibration offset of 0 dB for KaSACR observations. Cross-comparison  
1907 between KaSACR VPT mode and KAZR observations can then be used to quantify the KAZR  
1908 calibration offset trend. Since KaSACR and KAZR operate at the same frequency, this cross-  
1909 comparison uses full-profile samples rather than measurements at a specific height level, as  
1910 cumulative gaseous and rain attenuation should be consistent across range gates.

**Deleted:** mentioned ...reviously mentioned, KaSACR calibration offsets are...ained stable between May and September of ...022. Furthermore, its calibration offsets, calculated from the WRA fitting technique with the scanning VPT and stationary VPT measurements in Figure...ig. 6, are approximately -0.9 to -0.1 dB, respectively, and 1dB...round 1 dB from the...direct disdrometer comparison at light rain onset. We tentatively assign 0 dB... calibration offset of 0 dB for KaSACR observations. Then cross...ross-comparison between KaSACR VPT mode and KAZR observations can also...hen be used to quantify the KAZR calibration offset trend. As...ince KaSACR and KAZR operate at the same frequency, this cross-comparison is done with...ses full-profile samples rather than measurements at certain... specific height level since the... as cumulative gaseous and rain attenuation should be same at each...onsistent across range gate. (... [191])

**Formatted:** Space After: 6 pt

1911 For this cross-comparison, we first match the closest KaSACR profiles to KAZR profiles  
1912 and interpolate KaSACR height ranges to align with KAZR height ranges. We then select data  
1913 samples using a signal-to-noise ratio threshold of 5 dB for both KaSACR and KAZR. In

**Deleted:** allocate...atch the closest KaSACR profiles to KAZR profiles and interpolate the ...aSACR height range...anges to the...lign with KAZR height range. Then, we ...anges. We then select the ...ata sample (... [192])

2014 precipitating events, KaSACR in scanning VPT mode is expected to exhibit a sawtooth or  
2015 modulated WRA cycling behavior, while KAZR VPT operates under consistent/continuous WRA  
2016 (see Fig. 2). We categorize the collocated profiles into precipitating and non-precipitating periods  
2017 using collocated surface rain rates from disdrometer measurements. Finally, the daily mean offsets  
2018 between KaSACR and KAZR observations in non-precipitating clouds are calculated and shown  
2019 in Fig. 8b (red diamonds). These calculated offsets display a trend similar to that observed from  
2020 the WRA fitting technique against RWP measurements in Fig. 8b, further supporting the validity  
2021 of the WRA calibration offset behaviors and strengthening confidence in the offset drift observed  
2022 at the end of the campaign.

2023 To extend the method to different disdrometer setups, we applied the WRA fitting  
2024 technique to LDISQUANTS estimates. Additionally, we tested sensitivity to fitting functions of  
2025 log-linear and  $R^{1/3}$  dependencies to account for potential discrepancies. Figure 9 presents the  
2026 results with a 2-day running average. The daily calibration offsets show slight variation between  
2027 LDISQUANTS and VDISQUANTS, indicating minor differences in disdrometer measurements.  
2028 While the calibration offsets from the log-linear and  $R^{1/3}$  fittings can differ by up to 2 dB for  
2029 certain day, the overall trends remain similar, with a mean offset of approximately 2 dB before  
2030 July 2022, increasing to around 7 dB afterward.

## 2031

### 2032 5 Summary

2033 In this study, we have demonstrated the wet radome influence on Ka-band radar  
2034 observations through comparisons that included KaSACR VPT observations under scanning (that  
2035 may shed water buildup) and stationary (non-shedding) conditions. The WRA is attributed to both  
2036 wet film and cumulative rainwater collecting on the radar radome. This attenuation influence  
2037 increases, as the rain rate increases. In campaign settings, it was found this attenuation may exceed  
2038 10 dB under a modest rain rate of 5 mm hr<sup>-1</sup>. Taking advantage of the intrinsic WRA dependence  
2039 on rain rates as obtained in moderate rain events from the AMF1 deployment in Houston, TX  
2040 during the TRACER field campaign, a new relative calibration monitoring technique was  
2041 developed for use with the ARM KAZR (or similar cloud radar systems) observations.

2042 The well-correlated relation between  $Dze$  and  $R$  (in logarithmic space) on precipitating  
2043 days is fitted with a log-linear equation. This rain dependence of WRA serves as the basis for this

Deleted: the

Deleted: have

Deleted: the

Deleted: is

Deleted: a

Deleted:

Deleted: screen

Deleted: time

Deleted: the

Deleted: rate

Deleted: We find these

Deleted: have

Deleted: very

Deleted: trend

Deleted: those

Deleted: measurement

Deleted: . This

Deleted: supports

Deleted: viability

Deleted: we

Deleted:

Formatted: Space After: 6 pt

Formatted: Font: Times New Roman, Not Italic, Font colour: Text 1

Formatted: Space Before: 0 pt, After: 6 pt

Deleted: as obtained in moderate rain events from the AMF1 deployment in Houston, TX during the TRACER field campaign.

Deleted: , which has a similar tendency as the published WRA in Frasier et al. (2013) and Gorgucci et al. (2013). This behavior

2071 relative WRA calibration technique. The corrected KAZR  $Z_e$  with fitted  $Dze$ , which includes the  
2072 WRA and  $Z_e$  offset, agrees very well with both disdrometer-estimated and RWP-measured  $Z_e$ .  
2073 The radar calibration offset is calculated from the fitted  $Dze$  - $R$  relation when  $R$  equals 0.05 mm  
2074  $\text{hr}^{-1}$ , assuming WRA is negligible at this light rain rate. The daily fitted slopes over the course of  
2075 the TRACER campaign vary between 6 and 10 due to different data sampling in different rain  
2076 types. A slope sensitivity study suggests that the calibration offset deviations due to slope variation  
2077 are likely within the standard deviation of the estimated  $Z_e$  as function of  $R$ , as well as those typical  
2078 of underlying/collocated disdrometer measurement uncertainty (i.e.  $\sim 2$ -3 dB). The KAZR  
2079 calibration offsets calculated with a constant slope of 8 during the TRACER campaign are stable  
2080 near 2 dB compared to the disdrometer estimate with a standard deviation of 3 dB through June  
2081 2022. After that time, the calibration offsets increase to more than 7 dB.

2082 The performance of the WRA fitting calibration technique is evaluated by comparing it  
2083 with direct disdrometer measurements at the onset of rain events. The wet-radome technique  
2084 consistently identifies a sound calibration offset over the entire project and arguably outperforms  
2085 the direct disdrometer and radar comparison at the onset of light rain by reducing noise and  
2086 increasing temporal consistency. The WRA fitting calibration technique is also applied to the  
2087 KAZR observation against the calibrated RWP  $Z_e$  reference. This test reveals sound performance  
2088 and a clear and smooth matching trend in the July to September change in TRACER KAZR offsets,  
2089 indicating that the new technique can be applicable to other calibrated reference radars with  
2090 collocated surface rain rate measurements. The KAZR offset assessed from the cross-comparison  
2091 between the stable and calibrated KaSACR VPT mode and KAZR observations in non-  
2092 precipitating clouds also agree with the calibration offset trend from the WRA fitting technique.  
2093 The dialy calibration offsets varies due to the uncertainty of disdrometer measurements and the  
2094 fitting function of WRA, However the generally long-term trend from the WRA fitting technique  
2095 seens robust.

2096  
2097 Determining the calibration offset and monitoring the long-term trend of ARM KAZR is  
2098 the first step towards studying cloud seasonal and inter-seasonal variation. Having an easily  
2099 adjustable cloud radar calibration method with collocated disdrometer or RWP data available will  
2100 also facilitate cloud microphysical property retrieval, cloud process studies, and cloud variation  
2101 associated with climate change using ARM KAZR measurements. This technique has the

Deleted: Moreover, determining

Formatted: No underline

2|103 advantage of utilizing data from a broader range of light and moderate rain cases, avoiding the  
2|104 stringent requirements of other shorter-wavelength radar monitoring methods, which often rely on  
2|105 disdrometers or other radars and require observations of cloud, drizzle, or light rain at the onset of  
2|106 precipitation. Future plans include testing this newly developed WRA technique at other ARM  
2|107 fixed sites (e.g., in more humid, marine, or oceanic environments) to assess the extent of any  
2|108 necessary site-specific refinements for different radar and sampling conditions. Recently, this  
2|109 WRA monitoring technique has been applied to data from other ARM field campaigns, such as  
2|110 the Surface Atmosphere Integrated Field Laboratory (SAIL) and the Eastern Pacific Cloud Aerosol  
2|111 Precipitation Experiment (EPCAPE). Alongside TRACER, the offset trends derived from these  
2|112 three campaigns have shown favorable agreement with results from other independent KAZR  
2|113 calibration techniques documented in ARM radar b1 data processing reports (Feng et al., 2024;  
2|114 Matthew et al., 2024; Rocque et al., 2024).

**Deleted:** Since the technique may consider data samples collected during a wider range of light or moderate rain cases, it has a far less stringent requirement that other shorter-wavelength radar monitoring concepts using disdrometers or other radars that necessitate cloud, drizzle or light rain observations at rain onset. One plan is to test whether this newly developed WRA technique may be applicable to other cloud radars at ARM fixed sites (i.e., those in more/less humid, marine and/or oceanic environments), or to what extent further site-specific refinement is needed for different radar and sampling parameters. Recently, this WRA monitoring technique has been applied to measurements during other ARM field campaigns such as surface atmosphere integrated field laboratory (SAIL) and eastern pacific cloud aerosol precipitation experiment (EPCAPE). Along with TRACER, the resulted offset trends from those three campaigns are evaluated favorably with the results from other KAZR calibration technique done independently in ARM radar b1 data processing reports (Feng et al 2024, Matthew et al. 2024, Rocque et al 2024).

**Formatted:** Font: Not Bold, Font colour: Text 1

**Formatted:** Line spacing: 1.5 lines

2|155 Table 1. List of parameters for KAZR GE mode, KaSACR/XSACR in vertical pointing (VPT)  
 2|156 mode, and RWP in precipitation mode.

2|157

	<u>KAZR (GE mode)</u>	<u>KaSACR (VPT mode)</u>	<u>XSACR (VPT mode)</u>	<u>RWP (Precipitation mode)</u>
<u>Frequency (GHz)</u>	<u>34.0</u>	<u>35.3</u>	<u>9.71</u>	<u>1.29</u>
<u>Wavelength</u>	<u>8.57mm</u>	<u>8.50mm</u>	<u>3.09cm</u>	<u>23.3cm</u>
<u>Beam width (degree)</u>	<u>0.3</u>	<u>0.3</u>	<u>1.0</u>	<u>&gt;3</u>
<u>Time resolution (s)</u>	<u>2</u>	<u>4</u>	<u>3</u>	<u>5-8</u>
<u>Range resolution (m)</u>	<u>30</u>	<u>25</u>	<u>25</u>	<u>225</u>
<u>Minimum range (m)</u>	<u>160</u>	<u>Others: 428</u> <u>0903/04: 453</u>	<u>288</u>	<u>335</u>
<u>Radome diameter (m)</u>	<u>1.82</u>	<u>1.82</u>	<u>1.82</u>	<u>N/A</u>

2|158  
 2|159  
 2|160  
 2|161  
 2|162  
 2|163  
 2|164  
 2|165  
 2|166  
 2|167  
 2|168  
 2|169  
 2|170  
 2|171  
 2|172  
 2|173  
 2|174  
 2|175  
 2|176  
 2|177  
 2|178  
 2|179  
 2|180

Formatted: Font: Not Bold  
 Formatted: Line spacing: 1.5 lines

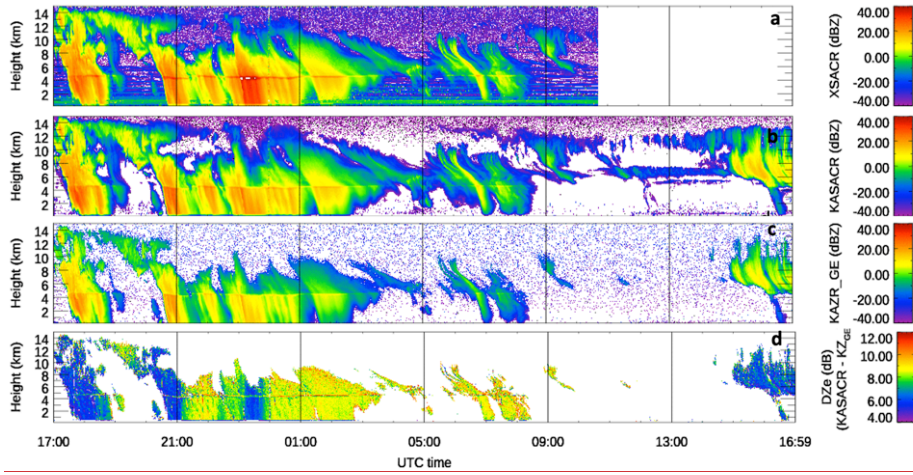
2181 Table 2. Sensitivity study of the slope value in the log-linear fitting for KAZR and KaSACR  
 2182 calibration on 03-04 September 2022 case in Figure 1.  $b$  and  $a$  are the slope and constant,  
 2183 respectively, in the log-linear fitting in Eq. 2.  $D_{Ze}(R=0.05)$  is the radar calibration offset when rain  
 2184 rate ( $R$ ) equals  $0.05 \text{ mm hr}^{-1}$ . More details can be found in Section 3.3.

**Deleted:** Table 2. Temperature measurements at different locations highlighted in Figure 1 from different resources, which includes ARM TRACER AMF1 MET, ozonesonde and boat measurements from TRACER – Air Quality 2 (TRACER-AQ2), and buoy data from the National data buoy center and NOAA weather service.

$b$	KAZR				KaSACR			
	$a$	$D_{Ze}$ ( $R=0.05$ )	Correlation coefficient ( $rr$ )	Standard deviation (dB)	$a$	$D_{Ze}$ ( $R=0.05$ )	Correlation coefficient ( $rr$ )	Standard deviation (dB)
6	17.1	9.3	0.88	3.8	9.8	2.0	0.89	3.4
8	18.1	7.7	0.90	3.9	10.9	0.5	0.91	3.4
8.6	18.5	7.3	0.91	4.1	11.1	-0.1	0.92	3.5
10	19.1	6.3	0.92	4.4	12.0	-1.0	0.93	3.7

2186  
2187  
2188  
2189  
2190  
2191  
2192  
2193  
2194  
2195  
2196  
2197  
2198  
2199

**Deleted: T (K)** ... [193]

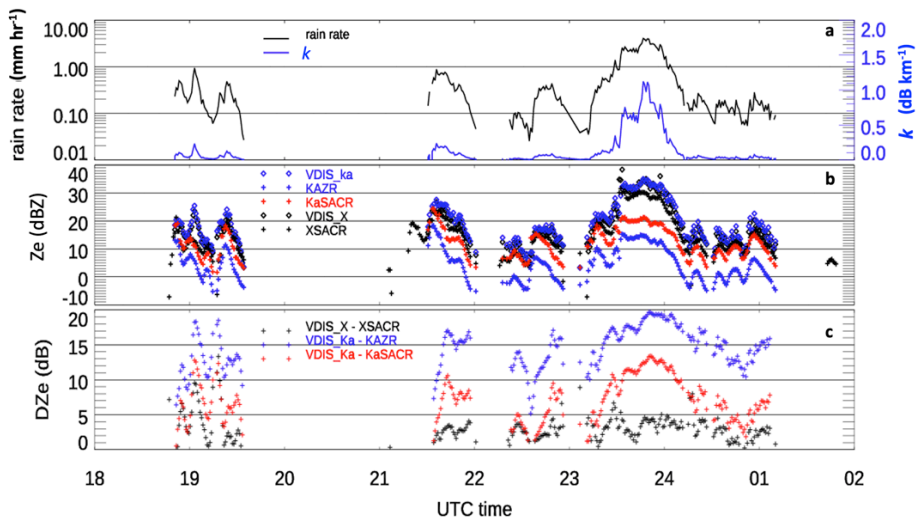


2209  
 2210 Figure 1. Measured radar reflectivity on 03-04 September 2022 from the TRACER field campaign.  
 2211 a) XSACR, missing data after 10:40 UTC on 04 September 2022, b) KaSACR, c) KAZR GE mode,  
 2212 d) Ze difference (DZe) between the KaSACR and the KAZR GE mode.

Deleted: Map around

Formatted: Font: Not Bold

2209  
 2210  
 2211  
 2212  
 2213  
 2214  
 2215  
 2216  
 2217  
 2218



2220  
 2221  
 2222 **Figure 2.** Measurements and comparison on 03-04 September 2022 between VDISQUANTS and  
 2223 radars. a) the timeseries of VDISQUANTS rain rate (black line) and rain droplet specific  
 2224 attenuation coefficients ( $K$ , blue line) at Ka band. b) the time series of measured Ze from KAZR  
 2225 GE (blue +), KaSACR (red +), and XSACR (black +) at 500 m after gaseous and rain attenuation  
 2226 corrections, and estimated Ze from VDISQUANTS at Ka (blue diamond) and X (black diamond)  
 2227 bands. c) Ze difference (DZe) between radar and disdrometer for XSACR (black cross), KaSACR  
 2228 (red cross), and KAZR (blue cross). For this case, SACR was operated in the stationary VPT  
 2229 mode.

Formatted: Line spacing: 1.5 lines

Deleted: AMF1 site

Formatted: Font: Not Bold

Deleted: La Porte

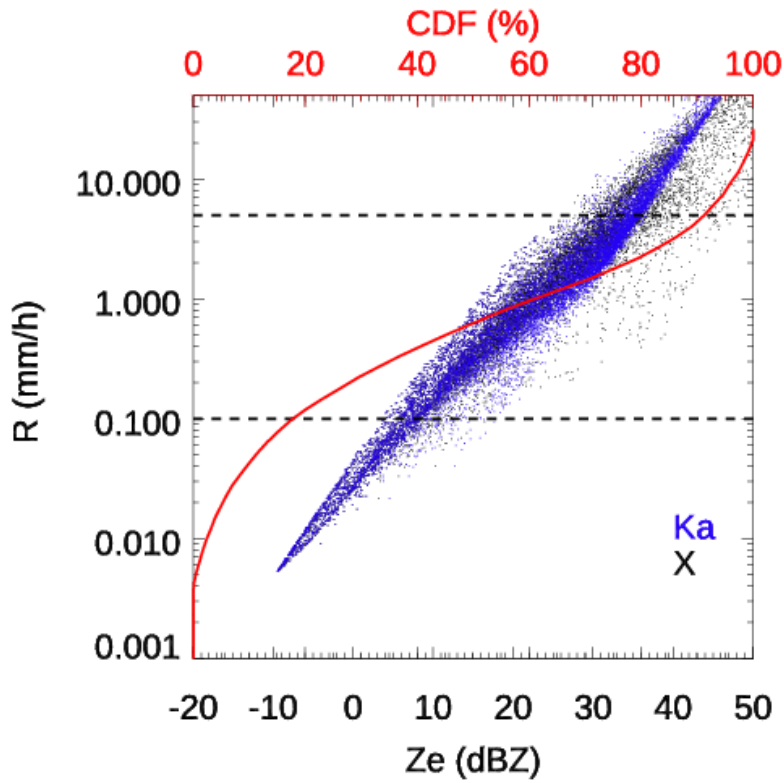
Deleted: dot)

Deleted: TRACER. Several sites are highlighted

Deleted: yellow dots



2248  
2249



2250

2251 Figure 3. The estimated Ze from VDISQUANTS for Ka (blue dots) and X bands (black dots)  
2252 during the entire TRACER campaign, plotted as a function of rain rate (R). The red line is the  
2253 cumulative probability function (CDF) of R. The two vertical black lines are at rain rates of 0.1  
2254 and 5.0 mm hr<sup>-1</sup>, respectively.

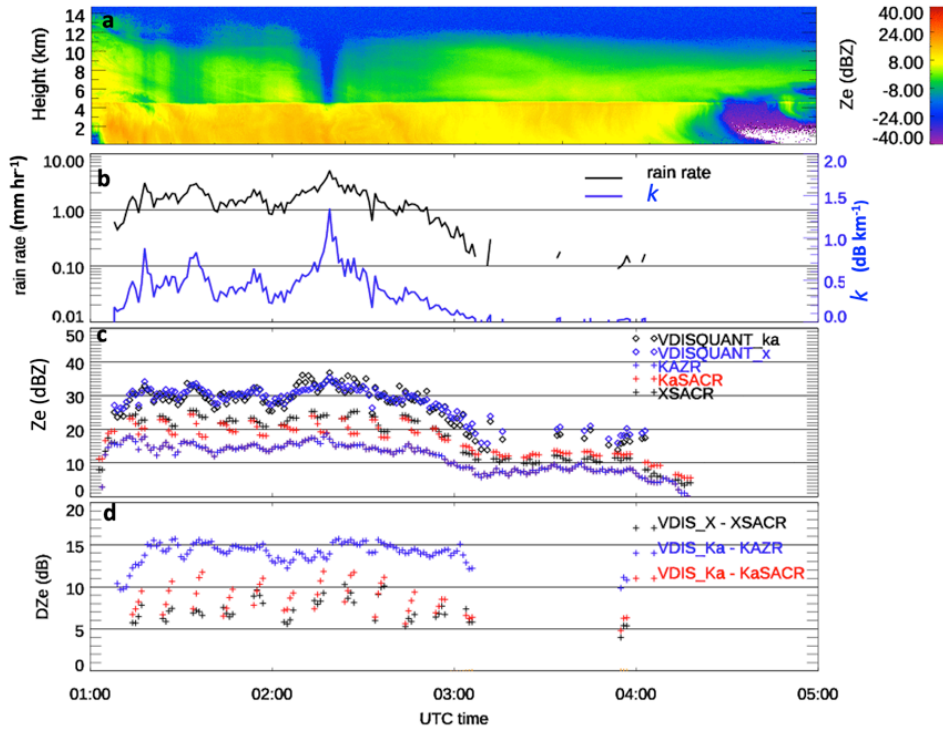
Formatted: Font colour: Text 1

Formatted: Normal (Web), Line spacing: 1.5 lines

2255

2256

Formatted: Font colour: Text 1



2257

2258 Figure 4. Radar and VDISQUANTS comparison for the case on August 11. a) Measured radar  
 2259 reflectivity ( $Z_e$ ) from the KAZR GE mode. b-d are similar to Fig. 2a-c. For this case, KaSACR  
 2260 and XSACR measurements are the scanning VPT mode and collocated with the VDISQUANTS  
 2261 with a  $\pm 2$  minutes averaging window.

2262

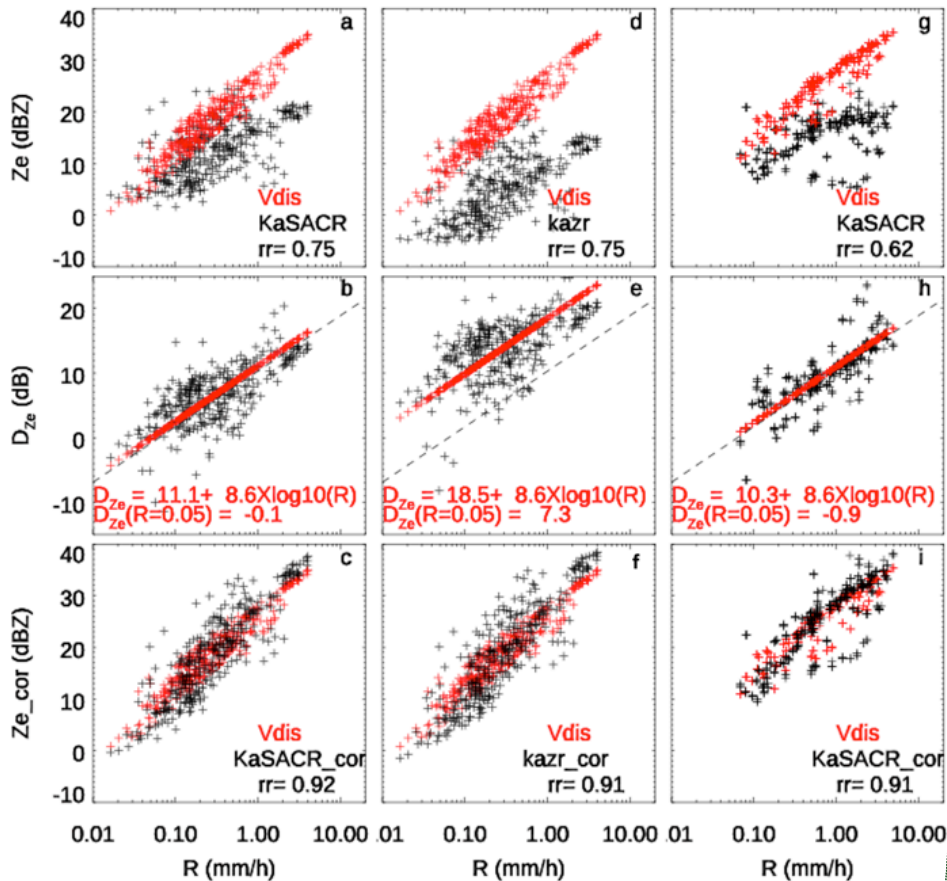
Deleted: temperature

Formatted: Normal (Web), Line spacing: 1.5 lines

Deleted: taken and listed in Table 2 to illustrate temperature gradients from Houston to Galveston Bay. The XSACR domain is marked

Deleted: a red circle

Formatted: Font colour: Text 1



2268  
 2269 Figure 5. a) Scatter plot of radar measured  $Z_e$  (black cross) at 500 m and VDISQUANTS-estimated  
 2270  $Z_e$  (red cross) as a function of rain rate  $R$ , b) Difference between measured  $Z_e$  and VDISQUANTS-  
 2271 estimated  $Z_e$  ( $D_{ze}$  in black). The log-linear fitting in Eq.2 with slope  $b$  at 8.6 are plotted in red  
 2272 cross, c) Scatter plot of radar measured  $Z_e$  (black cross) after log-linear fitting correction along  
 2273 with the VDISQUANTS-estimated  $Z_e$  (red cross) for KaSACR stationary VPT (a-c) and KAZR  
 2274 GE (d-f) on 03-04 September, and KaSACR stationary VPT (g-i) collected on May 25, August 05,  
 2275 11, 19 and 29. The correlation coefficients between the measured  $Z_e$  and estimated  $Z_e$  ( $rr$ ) before

Moved up [1]:  
 Figure

Moved down [4]:  
 Acknowledgement

Moved down [5]:

We acknowledge the exceptional work of the radar engineering team and data mentor team for the close to 100% operation rate of KAZR during the TRACER campaign. We would like to thank the ARM TRACER team for the quality data of KaSACR, XSACR, disdrometer, RWP and interpolated sounding measurements. Contributions from Brookhaven National Laboratory co-authors were supported by the Atmospheric Radiation Measurement (ARM) Facility and the Atmospheric System Research (ASR) program of the Office of Biological and Environmental Research in the U. S. Department of Energy, Office of Science, through Contract No. DE-SC0012704. Dr. C.R. Williams and the RWP work is supported under ASR grant number DE-SC0021345. Pacific Northwest National Laboratory (PNNL) is operated by Battelle for the U. S. Department of Energy. The authors from PNNL are also supported by ARM through Contract No. DE-SC0015990.

Deleted:

[194]

Deleted: 5. The time derivatives (a, c, e) and range derivatives (b, d, f) of Vd in Figure 4 a, c, e in 120°, 180° and 90° directions. The BBF and GBF identified fr...

[195]

Deleted:

[196]

Deleted: Vertical cross-sections of the BBF and GBF. (a)  $Z_e$  and (b) Vd from the XSACR HSRHI scan in the boundary layer, captured at 30-minute intervals between 18:18 and 22:58 UTC. The dark blue (red) box highlights the

[197]

Formatted: Font: Not Bold

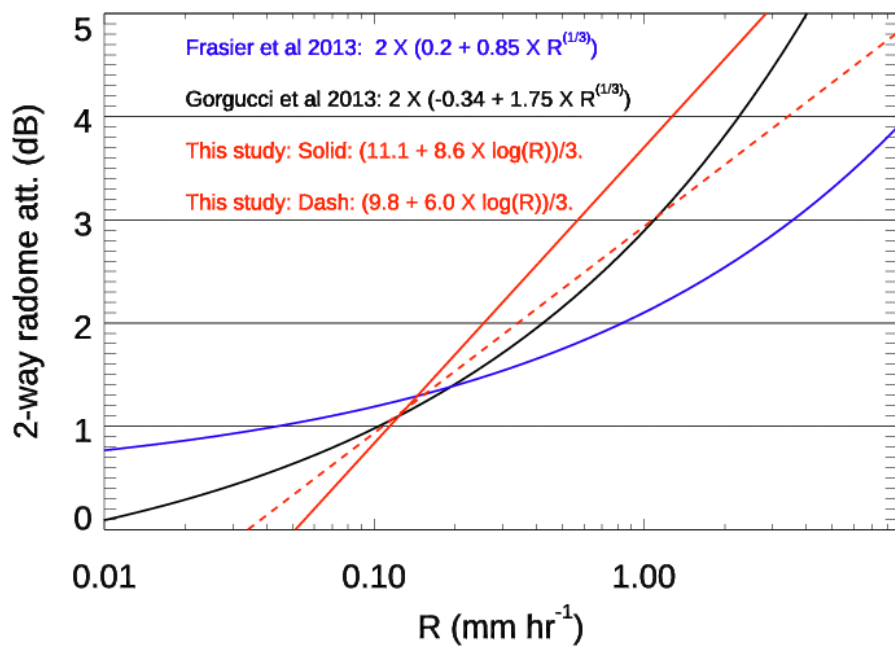
Formatted: Font colour: Text 1

Formatted: Font: Not Bold

Formatted: Font: (Default) Times New Roman, (Asian) Times New Roman, Not Italic, Font colour: Text 1

Formatted: Font: Not Bold

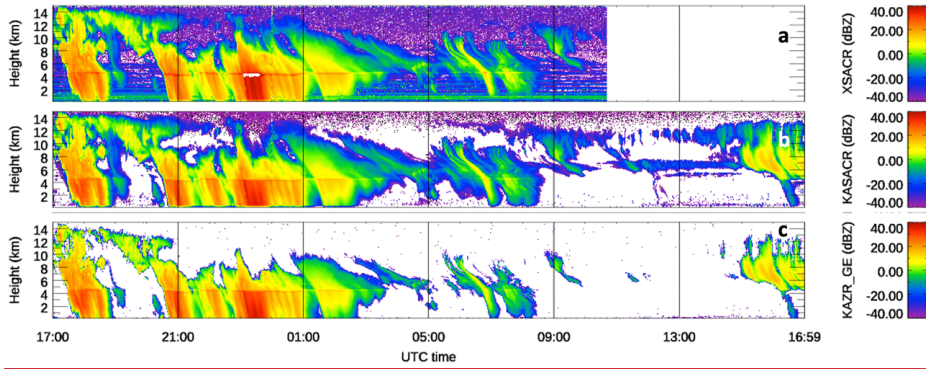
2436 and after the fitting correction are noted. The dashed black lines in second row (b, e, h) are the log-  
2437 linear fitting with  $a= 10.3$  and  $b= 8.6$  for KaSACR in Table 2.



2442

2443 Figure 6. Two-way radome attenuation as a function of rain rate ( $R$ ) using the log-linear WRA  
2444 fitting relation in Eq. 2 with slopes of 8.6 (solid red) and 6.0 (dashed red) in this study at Ka-band,  
2445 which is divided by 3 and compared with two previous studies about X-band radars from Frasier  
2446 et al. 2013 and Gorgucci et al. 2013.

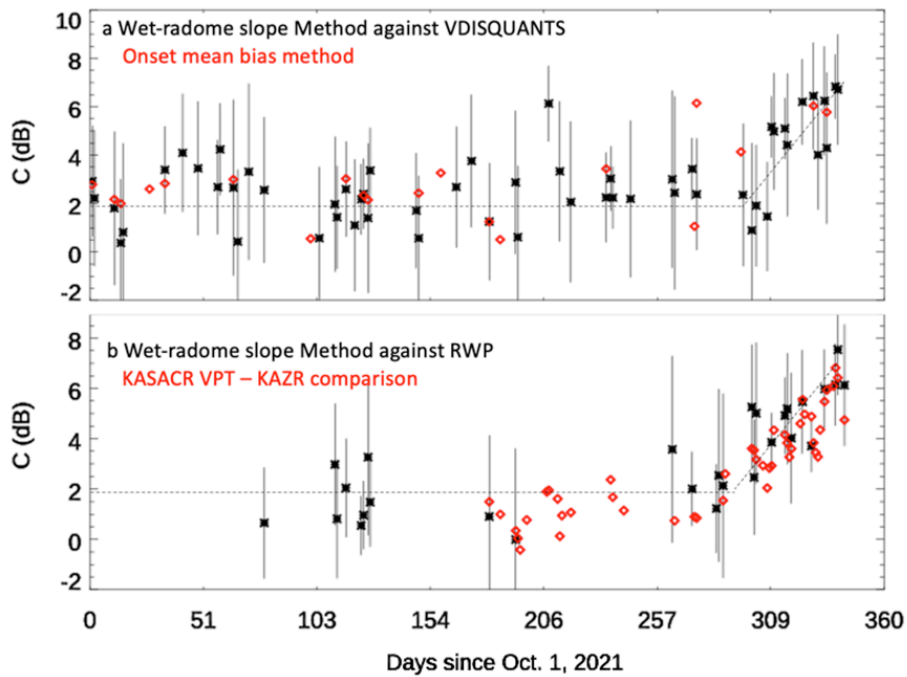
2447



2448  
2449  
2450  
2451  
2452  
2453  
2454  
2455  
2456  
2457

Figure 7. The same as Figure 1a-c except after WRA correction and radar calibration. For the precipitating period, KaSACR is corrected using Eq. 2, with a slope of 8.6 and constant of 11.1. XSACR is corrected with the offset of 3 dB from VDISQUANTs (black cross in Fig 2d), and KAZR GE mode is corrected using Eq. 2, with a slope of 8.6 and constant of 18.5. For non-precipitating periods, the calibration offsets of KaSACR and XSACR are assumed to be 0 dB, while the KAZR GE mode is calibrated with offset of 7 dB.

Deleted: ¶  
Formatted: Font: Not Bold

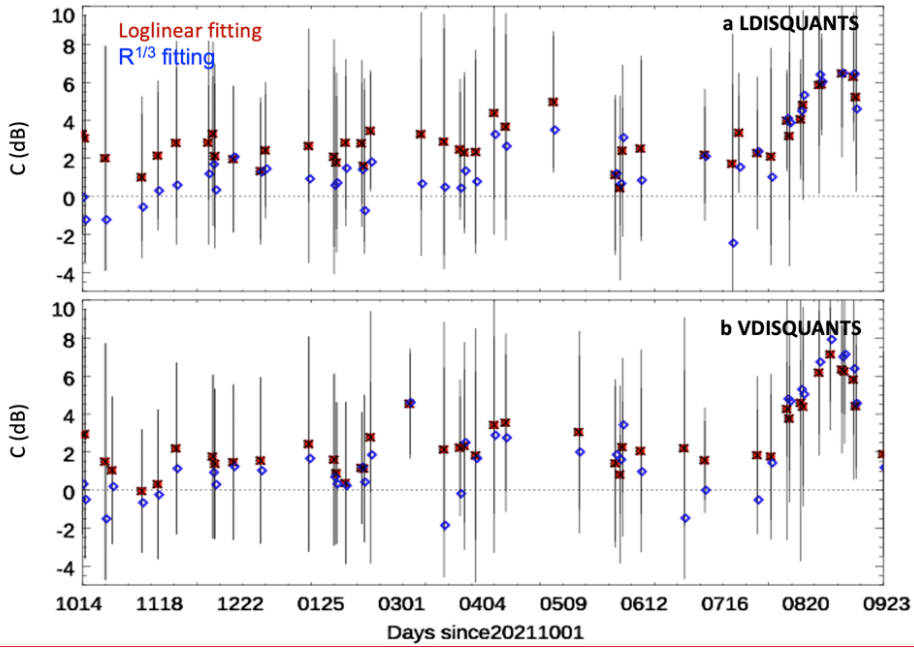


2469  
 2470  
 2471 Figure 8. a) KAZR daily calibration offsets ( $C$ ) from the mean KAZR bias method at the onset of  
 2472 light rain (red diamond) and the WRA fitting technique (black asterisk) against the VDISQUANTS  
 2473 data. Black vertical bar is the standard deviation of corrected  $Z_e$  against the estimated  $Z_e$ . b) KAZR  
 2474 daily calibration offset from the WRA fitting technique against the calibrated RWP measurement  
 2475 in black asterisk with vertical standard deviation bar. Red diamonds stand for the daily cross-  
 2476 comparison between the KaSACR VPT mode and the KAZR GE mode in non-precipitating clouds  
 2477 since May 26, 2022. The dashed black line is the mean trend outline from the WRA fitting  
 2478 technique in Fig. 8a.

2479

2480

2481



2482

2483 Figure 9 KAZR daily calibration offsets ( $C$ ) from loglinear fitting with Equation 1 (red asterisk  
 2484 with black standard deviation bar) or the  $R^{1/3}$  relation (blue diamond) against a) LDISQUANTS  
 2485 and b) VDISQUANTS data. The daily offsets are smoothed with 2-day window.

2486

2487

2488

2489

2490

2491

2492

Formatted: Font: Not Bold, Font colour: Auto

Formatted: Normal (Web)

2493 Data availability

2494 ▲ The KAZR, KaSACR and XSACR data at the TRACER campaign in this study are a1-level data.

2496 The surface disdrometer VDISQUANTS and interpolated sounding data are c1-level value added  
2497 product data. They are all available at ARM data discovery at <https://adc.arm.gov/discovery/#/> and  
2498 through the following DOIs. The calibrated radar wind profiler data is ARM PI product and can  
2499 be obtained from the data developer, Dr. Christopher R. Williams, through email  
2500 (christopher.williams@colorado.edu) contact.

2501  
2502 Bharadwaj, Nitin, Hardin, Joseph, Isom, Bradley, Johnson, Karen, Lindenmaier, Iosif, Matthews,  
2503 Alyssa, Nelson, Danny, Feng, Ya-Chien, Deng, Min, Rocque, Marquette, Castro, Vagner,  
2504 and Wendler, Tim. *Ka-Band Scanning ARM Cloud Radar*. United States: N. p., 2021. Web.  
2505 doi:10.5439/1469302.

2506 Bharadwaj, Nitin, Hardin, Joseph, Isom, Bradley, Johnson, Karen, Lindenmaier, Iosif, Matthews,  
2507 Alyssa, Nelson, Danny, Feng, Ya-Chien, Deng, Min, Wendler, Tim, Castro, Vagner, and  
2508 Rocque, Marquette. *X-Band Scanning ARM Cloud Radar*. United States: N. p., 2021. Web.  
2509 doi:10.5439/1469303.

2510 Hardin, Joseph, Giangrande, Scott, and Zhou, Aifang. *Idquants*. United States: N. p., 2019. Web.  
2511 doi:10.5439/1432694.

2512 Hardin, Joesph, Giangrande, Scott, Fairless, Tami, and Zhou, Aifang. *vdisquants: Video*  
2513 *Distrometer derived radar equivalent quantities. Retrievals from the VDIS instrument*  
2514 *providing radar equivalent quantities, including dual polarization radar quantities (e.g.,*  
2515 *Z, Differential Reflectivity ZDR)*. United States: N. p., 2021. Web. doi:10.5439/1592683.

2516 Isom, Bradley, Nelson, Danny, Andrei, Iosif, Hardin, Joseph, Matthews, Alyssa, Johnson, Karen,  
2517 Bharadwaj, Nitin, Feng, Ya-Chien, Rocque, Marquette, Deng, Min, Wendler, Tim, and  
2518 Castro, Vagner. *ARM: KAZRCFRGE*. United States: N. p., 2018. Web.  
2519 doi:10.5439/1498936.

2520 Isom, Bradley, Nelson, Danny, Andrei, Iosif, Hardin, Joseph, Matthews, Alyssa, Johnson, Karen,  
2521 Bharadwaj, Nitin, Feng, Ya-Chien, Rocque, Marquette, Deng, Min, Wendler, Tim, and  
2522 Castro, Vagner. *ARM: KAZRCFRMD*. United States: N. p., 2018. Web.  
2523 doi:10.5439/1498948.

Formatted: Font: Not Bold, Italic

Formatted: Normal



2524 Jensen, Michael, Giangrande, Scott, Fairless, Tami, and Zhou, Aifang. *interpolatedsonde*. United  
2525 States: N. p., 1998. Web. doi:10.5439/1095316.  
2526  
2527  
2528  
2529  
2530  
2531  
2532  
2533  
2534  
2535  
2536  
2537  
2538  
2539  
2540  
2541  
2542  
2543  
2544  
2545  
2546  
2547  
2548  
2549  
2550  
2551  
2552  
2553  
2554

2555 Author contribution  
2556 MD developed the main concept for the WRA calibration technique and led the manuscript  
2557 preparation. SG, MJ, and KJ contributed to the data analysis process. CW provided the  
2558 calibrated RWP data and contributed to its analysis and write-up. JC, YF, AM, MR, and  
2559 MD, as part of the ARM radar data mentor team, provided TRACER-related radar  
2560 information and additional KAZR calibration used in TRACER b1 data processing. IL and  
2561 TW, as ARM radar engineers, supplied critical information on radar hardware, software,  
2562 and radar saturation. AZ and DW contributed as the disdrometer mentors and VAP  
2563 developers. ZZ and EL provided valuable insights regarding radar wet radome attenuation.  
2564 All coauthors helped to edit and comment the manuscript draft.  
2565

2566 **Competing interests**

2567 The authors declare that they have no conflict of interest.  
2568

2569

2570

2571

2572

2573

2574

2575

2576

2577

2578

2579

2580

2581

2582

2583

2584

Deleted: ¶

Formatted: Font colour: Text 1, Pattern: Clear

Formatted: Indent: Left: 0", First line: 0"

Moved (insertion) [4]

2587 Acknowledgement

2588 We acknowledge the exceptional work of the radar engineering team and data mentor team for the  
2589 close to 100% operation rate of KAZR during the TRACER campaign. We would like to thank  
2590 the ARM TRACER team for the quality data of KaSACR, XSACR, disdrometer, RWP and  
2591 interpolated sounding measurements. Contributions from Brookhaven National Laboratory co-  
2592 authors were supported by the Atmospheric Radiation Measurement (ARM) Facility and the  
2593 Atmospheric System Research (ASR) program of the Office of Biological and Environmental  
2594 Research in the U. S. Department of Energy, Office of Science, through Contract No. DE-  
2595 SC0012704. Dr. C.R. Williams and the RWP work is supported under ASR grant number DE-  
2596 SC0021345. Pacific Northwest National Laboratory (PNNL) is operated by Battelle for the U. S.  
2597 Department of Energ. The authors from PNNL are also supported by ARM through Contract  
2598 No. DE-SC0015990.

Formatted: Font: Times New Roman, Not Italic, Font colour: Text 1

Formatted: Normal

2600 ▲  
2601 Reference

2602 Anderson, I., 1975: Measurements of 20-GHz transmission through a radome in rain. IEEE Trans.  
2603 Antennas Propag., 23, 619–622.

2604 Baldini, L., V. Chandrasekar, and Dmitri Moisseev 2012: Microwave radar signatures of  
2605 precipitation from S band to Ka band: application to GPM mission, International Journal  
2606 of Remote Sensing, Volume 41, 2020 - Issue 13, <https://doi.org/10.5721/EuJRS20124508>

2607 Bertie J. E.; Lan Z. (1996). "Infrared Intensities of Liquids XX: The Intensity of the OH Stretching  
2608 Band of Liquid Water Revisited, and the Best Current Values of the Optical Constants of  
2609 H2O(l) at 25°C between 15,000 and 1 cm<sup>-1</sup>". Applied Spectroscopy. 50 (8): 1047-  
2610 1057. doi:10.1366/0003702963905385. S2CID 97329854.

2611 Bringi, V. N, V Chandrasekar, N Balakrishnan, and DS Zrníc. 1990. "An Examination of  
2612 Propagation Effects in Rainfall on Radar Measurements at Microwave Frequencies."  
2613 Journal of Atmospheric and Oceanic Technologies 7(6): 829–840,  
2614 [https://doi.org/10.1175/1520-0426\(1990\)0072.0.CO;2](https://doi.org/10.1175/1520-0426(1990)0072.0.CO;2)

Formatted: Font: Not Bold

Deleted:

Formatted: Indent: Left: 0", First line: 0"

- 2616 Bringi, V. N., and Chandrasekar V., 2001: Polarimetric Doppler Weather Radar. Cambridge  
2617 University Press, 636 pp.
- 2618 Bechini, R., V. Chandrasekar, R. Cremonini, and S. Lim, 2010: Radome attenuation at X-band  
2619 radar operations. Proc. Sixth European Conf. on Radar in Meteorology and Hydrology,  
2620 Sibiu, Romania, ERAD, P15.1.
- 2621 Bringi, V. N, Kumar Vijay Mishra, Merhala Thurai, Patrick C. Kennedy, and Timothy H. Raupach  
2622 2020: Retrieval of Lower-Order Moments of the Drop Size Distribution using CSU-CHILL  
2623 X-band Polarimetric Radar: A Case Study. Atmospheric Measurement Techniques.  
2624 <https://doi.org/10.5194/amt-2020-160>
- 2625 Chandrasekar, V, L Baldini, N Bharadwaj, and PL Smith. Recommended Calibration Procedures  
2626 for GPM Ground Validation Radars, 103.
- 2627 Deng, M., and Pavlos Kollias, Zhe Feng, Chidong Zhang, Charles N. Long, Heike  
2628 Kalesse, Arunchandra Chandra, Vickal V. Kumar, and Alain Protat, 2014: Stratiform and  
2629 Convective Precipitation Observed by Multiple Radars during the DYNAMO/AMIE  
2630 Experiment. J. Appl. Meteor. Climatol., 53, 2503–2523, [https://doi.org/10.1175/JAMC-D-](https://doi.org/10.1175/JAMC-D-13-0311.1)  
2631 [13-0311.1](https://doi.org/10.1175/JAMC-D-13-0311.1).
- 2632 Feng, Y-C, A Matthews, M Rocque, M Deng, T Wendler, K Johnson, E Schuman, I Lindenmaier,  
2633 V Castro, SE Giangrande, S Collis, R Jackson, A Theisen, and J Comstock. 2024.  
2634 TRACER b1 Data Processing: Corrections, Calibrations, and Processing Report. U.S.  
2635 Department of Energy, Atmospheric Radiation Measurement user facility, Richland,  
2636 Washington. DOE/SC-ARM-TR-297.
- 2637 Frasier, S. J., F. Kabeche, J. Figueras i Ventura, H. Al-Sakka, P. Tabary, J. Beck, and O. Bousquet,  
2638 2013: In-Place Estimation of Wet Radome Attenuation at X Band. J. Atmos. Oceanic  
2639 Technol., 30, 917–928, <https://doi.org/10.1175/JTECH-D-12-00148.1>.
- 2640 Frech, M., Lange, B., Mammen, T., Seltmann, J., Morehead, C., & Rowan, J. (2013). Influence of  
2641 a Radome on Antenna Performance, Journal of Atmospheric and Oceanic

2642 Technology, 30(2), 313-324. Retrieved Mar 6, 2023,  
2643 from [https://journals.ametsoc.org/view/journals/atot/30/2/jtech-d-12-00033\\_1.xml](https://journals.ametsoc.org/view/journals/atot/30/2/jtech-d-12-00033_1.xml)

2644 Gibble, D., 1964: Effect of rain on transmission performance of a satellite communication system.  
2645 IEEE International Convention Record, Part VI, IEEE, 52.

2646 Giangrande, S. E., and A. V. Ryzhkov, 2005: Calibration of Dual-Polarization Radar in the  
2647 Presence of Partial Beam Blockage. *J. Atmos. Oceanic Technol.*, 22, 1156–1166,  
2648 <https://doi.org/10.1175/JTECH1766.1>.

2649 Giangrande, S. E., E. P. Luke and P. Kollias, 2010: Automated retrievals of precipitation  
2650 parameters using non-Rayleigh scattering at 95 GHz. *J. Atmos. Oceanic Technol.*, 27,  
2651 1490–1503.

2652 Giangrande, S. E., E. P. Luke, and P. Kollias, 2012: Characterization of Vertical Velocity and  
2653 Drop Size Distribution Parameters in Widespread Precipitation at ARM Facilities. *J. Appl.*  
2654 *Meteor. Climatol.*, 51, 380–391, <https://doi.org/10.1175/JAMC-D-10-05000.1>.

2655 Giangrande, S. E., S. Collis, J. Straka, A. Protat, C. Williams, and S. Krueger (2013), A summary  
2656 of convective-core vertical velocity properties using ARM UHF wind profilers in  
2657 Oklahoma, *J. Appl. Meteorol. Climatol.*, 52, 2278–2295.

2658 Giangrande, S. E., Toto, T., Jensen, M. P., Bartholomew, M. J., Feng, Z., Protat, A., Williams, C.  
2659 R., Schumacher, C., and Machado, L. (2016), Convective cloud vertical velocity and mass-  
2660 flux characteristics from radar wind profiler observations during GoAmazon2014/5, *J.*  
2661 *Geophys. Res. Atmos.*, 121, 12,891–12,913, doi:10.1002/2016JD025303.

2662 Giangrande, S. E., Wang, D., Bartholomew, M. J., Jensen, M. P., Mechem, D. B., Hardin, J. C., &  
2663 Wood, R. (2019). Midlatitude oceanic cloud and precipitation properties as sampled by the  
2664 ARM Eastern North Atlantic Observatory. *Journal of Geophysical Research: Atmospheres*,  
2665 124, 4741–4760. <https://doi.org/10.1029/2018JD029667>

2666 Goddard, J. W. F., Tan J., and Thurai M. , 1994: Technique for calibration of meteorological radar  
2667 using differential phase. *Electron. Lett.*, 30 , 166–167.

2668 Gorgucci, E., R. Bechini, L. Baldini, R. Cremonini, and V. Chandrasekar, 2013: The Influence of  
2669 Antenna Radome on Weather Radar Calibration and Its Real-Time Assessment. *J. Atmos.*  
2670 *Oceanic Technol.*, 30, 676–689, <https://doi.org/10.1175/JTECH-D-12-00071.1>.

2671 Dupont, J.C. M. A. Drouin, J.F. Ribaud, A. Gibe, J. Delanoe, F. Toledo, L. Pfitzenmaier, G.  
2672 Ghiggi, M. Schleiss: 2022 Hands-on training » on the monitoring of stability of DCR  
2673 reflectivity using disdrometers ACTRIS-CCRES workshop, November 14-15th 2022,  
2674 SIRTA Observatory.

2675  
2676 Hardin, J., A. Hunzinger, E. Schuman, A. Matthews, N. Bharadwaj, A. Varble, K. Johnson, and  
2677 S. Giangrande, 2020: CACTI Radar b1 Processing: Corrections, Calibrations, and  
2678 Processing Report. Tech. Doc. DOE/SC-ARM-  
2679 TR244, 46 pp., <https://arm.gov/publications/brochures/doe-sc-arm-tr-244.pdf>.

2680 Hardin, J., Giangrande, S. E., and Zhou, A. Laser Disdrometer Quantities (LDQUANTS) and  
2681 Video Disdrometer Quantities (VDISQUANTS) Value-Added Products Report. United  
2682 States: N. p., 2020. Web. doi:10.2172/1808573.

2683 Hunzinger, A, JC Hardin, N Bharadwaj, A Varble, and A Matthews. 2020. “An Extended Radar  
2684 Relative Calibration Adjustment (eRCA) Technique for Higher Frequency Radars and RHI  
2685 Scans.” *Atmospheric Measurement Techniques Discussions*, [https://doi.org/10.5194/amt-](https://doi.org/10.5194/amt-2020-57)  
2686 2020-57

2687 Jensen, M. P., D. Collins, P. Kollias, D. Rosenfeld, A. Varble, S. Collis, J. Fan, R. Griffin, R.  
2688 Jackson, T. Logan, G. McFarquhar, J. Quaas, R. Sheesley, P. Stier, S. van den Heever, Y.  
2689 Wang, G. Zhang, E. Bruning, A. Fridlind, C. Kuang, A. Ryzkhov, S. Brooks, . Defer, S.  
2690 E. Giangrande, J. Hu, M. Kumjian, T. Matsui, C. Nowotarski, M. Oue,, J. Snyder, S.  
2691 Usenko, M. van Lier Walqui, and Y. Xu, 2019: TRacking Aerosol Convection Interactions  
2692 Experiment (TRACER) Science Plan. DOE/SC-ARM-19-017. 30 pp.

2693 Jensen, M. P., L. Judd, P. Kollias, J. Sullivan, R. Nadkarni, C. Kuang, G. McFarquhar, H. Powers  
2694 and J. Flynn, 2022: A succession of cloud, precipitation, aerosol and air quality field

2695 experiments in the coastal urban environment. Bull. Amer. Meteor. Soc.,  
2696 <https://doi.org/10.1175/BAMS-D-21-0104.1>.

2697 Jensen, M. P., J. H. Flynn, P. Kollias, C. Kuang, G. McFarquhar, H. Powers, S. Brooks, E. Bruning,  
2698 D. Collins, S. M. Collis, J. Fan, A. Fridlind, S. E. Giangrande, R. Griffin, J. Hu, R. C.  
2699 Jackson, M. Kumjian, T. Logan, T. Matsui, C. Nowotarski, M. Oue, A. Rapp, D. Rosenfeld,  
2700 A. Ryzhkov, R. Sheesley, J. Snyder, P. Stier, S. Usenko, S. van den Heever, M. van Lier-  
2701 Walqui, A. Varble, Y. Wang, A. Aiken, M. Deng, D. Dexheimer, M. Dubey, Y. Feng, V.  
2702 Ghate, K. L. Johnson, K. Lamer, S. Saleeby, D. Wang, M. Zawadowicz and A. Zhou, 2023:  
2703 TRacking Aerosol Convection interactions ExpeRiment (TRACER) final campaign report.  
2704 DOE/SC-ARM-3-038. 132 pp.

2705  
2706 Kollias, P., Bharadwaj N., Widener K. , Jo I. , and Johnson K. , 2014a: Scanning ARM cloud  
2707 radars. Part I: Operational sampling strategies. J. Atmos. Oceanic Technology, in press.

2708 Kollias, P., and Coauthors, 2014b: Scanning ARM Cloud Radars. Part II: Data Quality Control  
2709 and Processing. J. Atmos. Oceanic Technol., 31, 583–  
2710 598, <https://doi.org/10.1175/JTECH-D-13-00045.1>.

2711 Kollias, P., E. E. Clothiaux, M. A. Miller, B. A. Albrecht, G. L. Stephens, and T. P. Ackerman,  
2712 2007: Millimeter-Wavelength Radars: New Frontier in Atmospheric Cloud and  
2713 Precipitation Research. Bull. Amer. Meteor. Soc., 88, 1608–  
2714 1624, <https://doi.org/10.1175/BAMS-88-10-1608>.

2715 Kollias, P., and Coauthors, 2020: The ARM Radar Network: At the Leading Edge of Cloud and  
2716 Precipitation Observations. Bull. Amer. Meteor. Soc., 101, E588–  
2717 E607, <https://doi.org/10.1175/BAMS-D-18-0288.1>.

2718 Kollias, P., B. P. Treserras, and A. Protat, 2019: Calibration of the 2007–2017 record of  
2719 Atmospheric Radiation Measurements cloud radar observations using CloudSat,  
2720 Atmospheric Measurement Techniques, 12, 4949–4964, [https://doi.org/10.5194/amt-12-](https://doi.org/10.5194/amt-12-4949-2019)  
2721 4949-2019

- 2722 Kurri, M., and A. Huuskonen, 2008: Measurements of the transmission loss of a radome at  
2723 different rain intensities. *J. Atmos. Oceanic Technol.*, 25, 1590–1599.
- 2724 Lamer, K., Mariko Oue, Alessandro Battaglia, Richard J. Roy, Ken B. Cooper, Ranvir  
2725 Dhillon, and Pavlos Kollias 2021: Multifrequency radar observations of clouds and  
2726 precipitation including the G-band. *Atmospheric Measurement Techniques*. Volume 14,  
2727 issue 5 *AMT*, 14, 3615–3629, 2021 <https://doi.org/10.5194/amt-14-3615-2021>
- 2728 Lhermitte, R., 2002: *Centimeter and Millimeter Wavelength Radars in Meteorology*. Lhermitte  
2729 Publications, 550 pp.
- 2730 Liu, Y. and Mace, G. G.: Assessing synergistic radar and radiometer capability in retrieving ice  
2731 cloud microphysics based on hybrid Bayesian algorithms, *Atmos. Meas. Tech.*, 15, 927–  
2732 944, <https://doi.org/10.5194/amt-15-927-2022>, 2022.
- 2733 Louf, V., A. Protat, R. A. Warren, S. M. Collis, D. B. Wolff, S. Raunyar, C. Jakob, and W. A.  
2734 Petersen, 2019: An Integrated Approach to Weather Radar Calibration and Monitoring  
2735 Using Ground Clutter and Satellite Comparisons. *J. Atmos. Oceanic Technol.*, 36, 17–  
2736 39, <https://doi.org/10.1175/JTECH-D-18-0007.1>.
- 2737 Luca Baldini, V. Chandrasekar & Dmitri Moisseev (2012) Microwave radar signatures of  
2738 precipitation from S band to Ka band: application to GPM mission, *European Journal of*  
2739 *Remote Sensing*, 45:1, 75-88, DOI: 10.5721/EuJRS20124508
- 2740 Maahn, M., Hoffmann, F., Shupe, M. D., de Boer, G., Matrosov, S. Y., and Luke, E. P.: Can liquid  
2741 cloud microphysical processes be used for vertically pointing cloud radar calibration?,  
2742 *Atmos. Meas. Tech.*, 12, 3151–3171, <https://doi.org/10.5194/amt-12-3151-2019>, 2019.
- 2743 Matrosov, S. Y., 2005: Attenuation-Based Estimates of Rainfall Rates Aloft with Vertically  
2744 Pointing Ka-Band Radars. *J. Atmos. Oceanic Technol.*, 22, 43–  
2745 54, <https://doi.org/10.1175/JTECH-1677.1>.



2746 Matthews, A., M. Deng, E. Schuman, Y.Feng, M. Rocque, 2024: SAIL Radar B1 Processing:  
 2747 Corrections, Calibrations, and Processing Report. U.S. Department of Energy,  
 2748 Atmospheric Radiation Measurement user facility, Richland, Washington. In preparation.

2749 Mead, J. 2010. MMCR Calibration Study. U.S. Department of Energy. DOE/SC-ARM/TR-088.

2750 Meagher, Jonathan P., and Ziad S. Haddad. "To What Extent Can Raindrop Size Be Determined  
 2751 by a Multiple-Frequency Radar?" *Journal of Applied Meteorology and Climatology*, vol.  
 2752 45, no. 4, 2006, pp. 529–36. JSTOR, <http://www.jstor.org/stable/26171702>. Accessed 13  
 2753 Mar. 2023.

2754 Miller, M. A., K. Nitschke, T. P. Ackerman, W. R. Ferrell, N. Hickmon, and M. Ivey, 2016: The  
 2755 ARM Mobile Facilities. *Meteor. Monogr.*, 57, 9.1–  
 2756 9.15, <https://doi.org/10.1175/AMSMONOGRAPHS-D-15-0051.1>.

2757 Muradyan, P, and Coulter, R.: Radar Wind Profiler (RWP) and Radio Acoustic Sounding System  
 2758 (RASS) instrument handbook, U. S. Department of Energy, Atmospheric Radiation  
 2759 Measurement user facility, DOE/SC-ARM-TR-044, <https://doi.org/10.2172/1020560>,  
 2760 2020.

2761 Myagkov, A., Kneifel, S., and Rose, T.: Evaluation of the reflectivity calibration of W-band radars  
 2762 based on observations in rain, *Atmos. Tech.*, 13, 5799–5825, [https://doi.org/10.5194/amt-](https://doi.org/10.5194/amt-13-5799-2020)  
 2763 [13-5799-2020](https://doi.org/10.5194/amt-13-5799-2020), 2020.

2764 Protat, A., D. Bouniol, E. J. O'Connor, H. Klein Baltink, J. Verlinde, and K. Widener, 2011:  
 2765 CloudSat as a Global Radar Calibrator. *J. Atmos. Oceanic Technol.*, 28, 445–452,  
 2766 <https://doi.org/10.1175/2010JTECHA1443.1>.

2767 Rocque, M. M. Deng, Y.Feng, E. Schuman, I. Silber, A. Matthews, T. Wendler, V. Castro, Iosif  
 2768 Lindenmaier, 2024: EPCAPE Radar b1 Processing: Corrections, Calibrations, and  
 2769 Processing Report, U.S. Department of Energy, Atmospheric Radiation Measurement user  
 2770 facility, Richland, Washington. In preparation.

Formatted: No underline, Font colour: Text 1

Formatted: No underline, Font colour: Text 1

Formatted: Font colour: Text 1

2771 Ryzhkov, AV, SE Giangrande, VM Melnikov, and TJ Schuur. 2005. "Calibration Issues of Dual-  
2772 Polarization Radar Measurements." *Journal of Atmospheric and Oceanic Technology*  
2773 22(8): 1138– 1155, <https://doi.org/10.1175/JTECH1772.1>.

Formatted: Hyperlink

2774 [Segelstein, D. J., "The complex refractive index of water," University of Missouri-Kansas City,](#)  
2775 [\(1981\).](#)

2776 Thompson, R., A. Illingworth, T. Darlington, and J. Ovens, 2012: Correcting attenuation in  
2777 operational radars from both heavy rain and the radome using the observed microwave  
2778 emission. *Proc. Seventh European Conf. on Radar in Meteorology and Hydrology,*  
2779 *Toulouse, France, ERAD, 8A.5.*

2780 Tridon, F., Battaglia, A., Kollias, P., Luke, E., and Williams, C. R.: Signal postprocessing and  
2781 reflectivity calibration of the Atmospheric Radiation Measurement Program 915-MHz  
2782 Wind Profilers, *J. Atmos. Ocean. Tech.*, 30, 1038-1054. [https://doi.org/10.1175/JTECH-](https://doi.org/10.1175/JTECH-D-12-00146.1)  
2783 [D-12-00146.1](https://doi.org/10.1175/JTECH-D-12-00146.1), 2013.

2784 Ulaby, F. T., R.K. Moore, and A.K. Fung, 1981: *Microwave Remote Sensing. Vol. 1, Addison-*  
2785 *Wesley, 456pp.*

2786 Varble, A. C., and Coauthors, 2021: Utilizing a Storm-Generating Hotspot to Study Convective  
2787 Cloud Transitions: The CACTI Experiment. *Bull. Amer. Meteor. Soc.*, 102, E1597–  
2788 E1620, <https://doi.org/10.1175/BAMS-D-20-0030.1>.

Formatted: Font: Not Bold

2789 Wang D, S Giangrande, M Bartholomew, J Hardin, Z Feng, R Thalman, and L Machado.  
2790 2018. "The Green Ocean: precipitation insights from the GoAmazon2014/5  
2791 experiment." *Atmospheric Chemistry and Physics*, 18(12), 10.5194/acp-18-9121-2018.

2792 Wang D, S Giangrande, Bartholomew, J Hardin 2021: Analysis of Three Types of Collocated  
2793 Disdrometer Measurements at the ARM Southern Great Plains Observatory, DOE/SC-  
2794 ARM-TR-275. <https://www.arm.gov/publications/programdocs/doe-sc-arm-tr-275.pdf>

2795 Widener, K. B. and J. B Mead 2004: *W-Band ARM Cloud Radar – Specifications and Design*

2796 Fourteenth ARM Science Team Meeting Proceedings, Albuquerque, New Mexico, March 22-26,

2797 Widener, K., N Bharadwaj, and K. Johnson, 2012: Ka-Band ARM Zenith Radar (KAZR)

2798 handbook. DOE/SC-ARM/TR-106

2799 [https://www.arm.gov/publications/tech\\_reports/handbooks/kazr\\_handbook.pdf](https://www.arm.gov/publications/tech_reports/handbooks/kazr_handbook.pdf)

2800 Wolff, DB, DA Marks, and WA Petersen. 2015. "General Application of the Relative Calibration

2801 Adjustment (RCA) Technique for Monitoring and Correcting Radar Reflectivity

2802 Calibration." *Journal of Atmospheric and Oceanic Technology* 32(3): 496–506,

2803 <https://doi.org/10.1175/JTECH-D-13-00185.1>

2804 Williams, C. R., Gage, K. S., Clark, W., and Kucera, P.: Monitoring the reflectivity calibration of

2805 a scanning radar using a profiling radar and a disdrometer, *J. Atmos. Oceanic Technol.*, 22,

2806 1004-1018, 2005.

2807 Williams, C.R., Barrio, J., Johnston, J. E., Myradyan, P. and Giangrande, S. E.: Calibrating radar

2808 wind profiler reflectivity factor using surface disdrometer observations, *J. Atmos. Meas.*

2809 *Techn.*, in review, <https://egusphere.copernicus.org/preprints/2023/egusphere-2022-1405>,

2810 2023.

2811 Xingjian Yu, Yu Zhang, Run Hu, Xiaobing Luo, 2021: Water droplet bouncing dynamics, *Nano*

2812 *Energy*, Volume 81, 2021, 105647, ISSN 2211-

2813 2855, <https://doi.org/10.1016/j.nanoen.2020.105647>.

2814 Zhang, G., J. Vivekanandan and E. Brandes, "A method for estimating rain rate and drop size

2815 distribution from polarimetric radar measurements," in *IEEE Transactions on Geoscience*

2816 *and Remote Sensing*, vol. 39, no. 4, pp. 830-841, April 2001, doi: 10.1109/36.917906.

2817 Zhu, Z., Lamer, K., Kollias, P., & Clothiaux, E. E. (2019). The vertical structure of liquid water

2818 content in shallow clouds as retrieved from dual-wavelength radar observations. *Journal of*

2819 *Geophysical Research:*

2820 *Atmospheres*, 2019; 124: 14184– 14197. <https://doi.org/10.1029/2019JD031188>

2821